remote sensing

MDPI

Article

High-Resolution 3D Structural Documentation of the Saqqara Pyramids, Egypt, Using Terrestrial Laser Scanning and Integrated Geomatics Techniques for Heritage Preservation

Abdelhamid Elbshbeshi [1], Abdelmonem Mohamed [1] and Ismael M. Ibraheem [2,*]

[1] Geodynamic Department, National Research Institute of Astronomy and Geophysics (NRIAG), Helwan 11722, Egypt; abdelhamid_mohammed@nriag.sci.eg (A.E.); abdelmonem@nriag.sci.eg (A.M.)
[2] Institute of Geophysics and Meteorology, University of Cologne, Pohligstrasse 3, 50969 Cologne, Germany
* Correspondence: ismael.ibraheem@geo.uni-koeln.de

Highlights

What are the main findings?

- Integrated Terrestrial Laser Scanning (TLS), GNSS, and Total Station techniques produced sub-centimeter georeferenced 3D models of the Djoser, Unas, Teti, and Userkaf pyramids, generating over 2.1 billion high-resolution points with registration errors below 4 mm.
- Quantitative analysis revealed major structural degradation, including height losses of ~53% (Unas), ~66% (Teti), and ~63% (Userkaf), and localized deformation up to 4.2 cm at Teti's southern flank.

What are the implications of the main findings?

- The generated georeferenced digital twins establish an accurate baseline for long-term deformation monitoring, structural stability assessment, and climate-related risk evaluation at large archaeological sites.
- The integrated geomatics workflow provides a scalable and transferable framework for high-precision documentation and conservation planning of complex heritage structures worldwide.

Abstract

Accurate 3D documentation of large and complex structures is essential for long-term stability assessment, structural monitoring, and conservation planning, particularly for heritage sites exposed to environmental and anthropogenic threats. This study develops an integrated workflow combining Terrestrial Laser Scanning (TLS), Global Navigation Satellite System (GNSS), and Total Station geodetic control for large-scale, high-precision documentation. The approach was implemented at the Saqqara archaeological zone, a UNESCO World Heritage Site facing significant deterioration risks, to document four major pyramids: Djoser, Unas, Teti, and Userkaf. More than 2.1 billion georeferenced points were acquired from 16 scan positions with sub-centimeter registration errors and overall geometric accuracy better than ±1 cm. From these datasets, detailed mesh models, orthoimages, Digital Elevation Models (DEMs), contour maps, and 2D plans were derived. These enabled quantitative analyses of height loss and volumetric change, indicating severe structural degradation in Unas (~53%), Teti (~66%), and Userkaf (~63%), as well as localized deformations such as 4.2 cm displacement at Teti's south flank. The degradation results from environmental factors and anthropogenic influences. Beyond this case study, the workflow proves that integrated TLS documentation can be applied to large and

Check for updates

Academic Editors: Jie He, Fulong Chen and Massimiliano Pepe

Received: 1 March 2026
Revised: 5 April 2026
Accepted: 8 April 2026
Published: 11 April 2026

Copyright: © 2026 by the authors. Licensee MDPI, Basel, Switzerland. This article is an open access article distributed under the terms and conditions of the Creative Commons Attribution (CC BY) license.

complex structures, supporting deformation monitoring, stability assessment, and digital twin development.

Keywords: terrestrial laser scanning (TLS); 3D heritage documentation; Saqqara pyramids; Egypt; cultural heritage preservation; digital archaeology

1. Introduction

Preserving cultural heritage sites is crucial for maintaining historical identity, supporting archaeological research, and promoting sustainable tourism. Yet, many monuments worldwide are increasingly threatened by environmental change, urban development, and human activities. Accurate documentation and continuous monitoring are therefore essential to ensure their long-term protection and to support informed conservation strategies [1–5]. Saqqara, as one of Egypt's most important archaeological zones and a UNESCO World Heritage Site (Figure 1), faces many of these same challenges, making its systematic digital documentation a matter of both national and international significance.

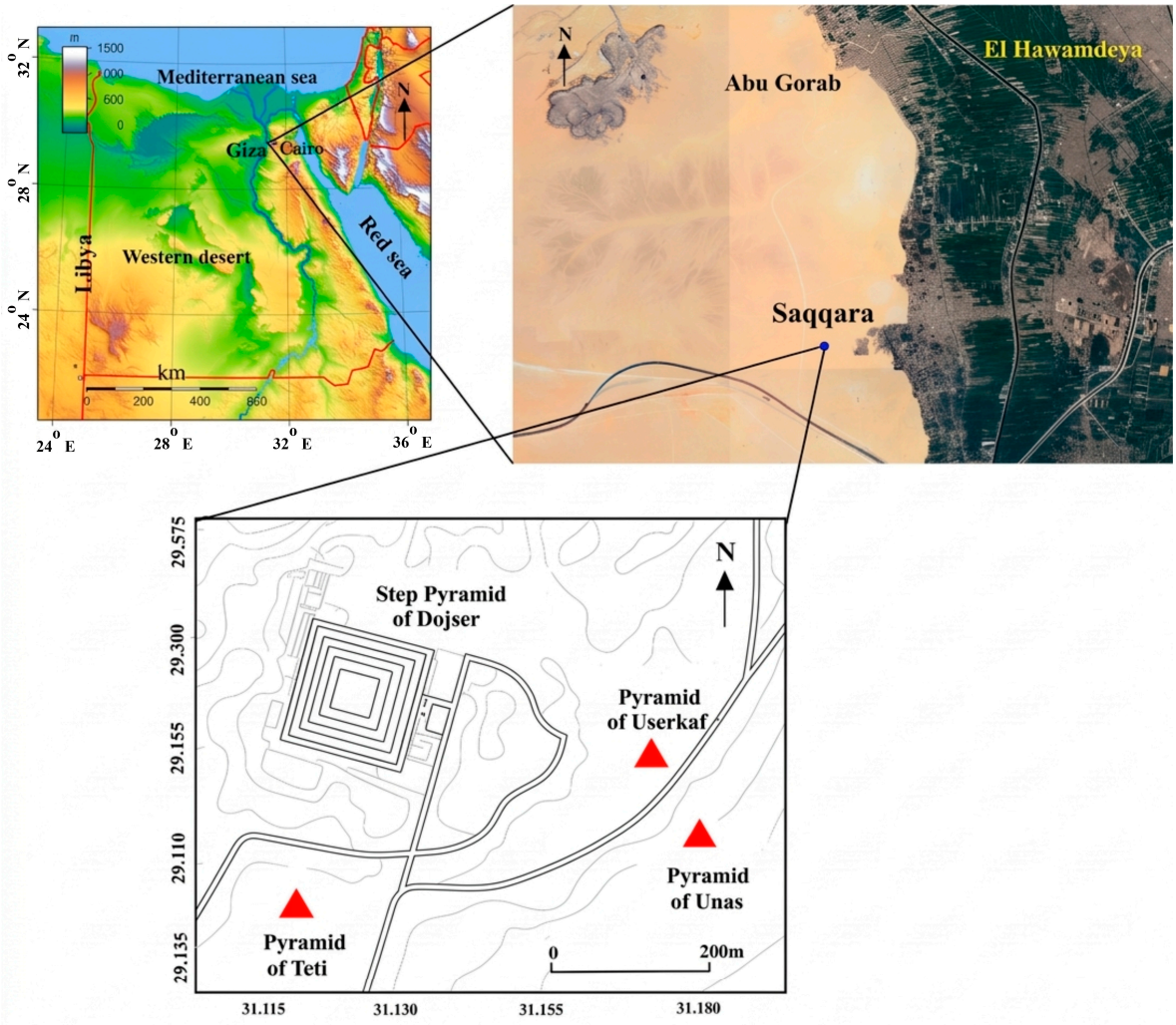

Figure 1. Location map of the Saqqara Necropolis, Egypt. **The upper-left** panel shows the position of Saqqara within the Nile Valley, between the Western Desert and the Red Sea. **The upper-right** panel presents a satellite image illustrating its proximity to Abu Gorab and El Hawamdeya. **The lower** panel provides a detailed map of the Saqqara archaeological zone, showing the Step Pyramid of Djoser and the pyramids of Teti, Userkaf, and Unas, with the latter three indicated by red triangles.

The Saqqara archaeological zone, located approximately 20 km south of Cairo on the western bank of the Nile, forms the heart of the Memphis Necropolis. Serving as the principal royal cemetery during Egypt's Early Dynastic and Old Kingdom periods, Saqqara hosts a unique concentration of monumental architecture, most notably the Step Pyramid of Djoser, regarded as the world's first large-scale cut-stone construction [6]. In addition to Djoser's complex, designed by Imhotep around 2670 BCE, the site features the pyramids of Unas, Teti, and Userkaf (Figure 1), as well as mastabas, temples, and later burials spanning more than three millennia of Egyptian history [7]. The site has been the subject of systematic archaeological investigation since the nineteenth century, with foundational architectural documentation provided by Lauer [8] and ongoing international excavation and research programs continuing to reveal new aspects of its historical significance [9,10]. This uninterrupted record makes Saqqara an unparalleled archive of ancient religious, architectural, and sociopolitical developments.

Despite its outstanding value, Saqqara faces a convergence of environmental and anthropogenic threats that pose serious risks to its long-term preservation. These include wind erosion, salt crystallization, thermal stress from temperature fluctuations, seismic activity, and rising groundwater levels (Figure 2) [11,12]. In addition, decades of uncontrolled tourism, rapid urbanization, and environmental pollution have accelerated the physical degradation of key monuments. The limestone used in many of these structures is particularly vulnerable, with numerous blocks showing advanced signs of cracking, flaking, and surface erosion [13]. Given the site's vast extent, the diversity of structural conditions, and limited conservation resources, large areas of Saqqara remain inadequately documented, leaving heritage professionals without the baseline data required for effective monitoring, maintenance, and emergency intervention [14].

Over millennia, many of the Saqqara pyramids have undergone substantial height reduction, exposing them to growing environmental threats. These structures have lost significant vertical extent ranging from several meters to tens of meters due to climate-driven erosion processes, salt weathering, and human exploitation. For instance, the upper casing stones of the Step Pyramid have suffered accelerated deterioration caused by salt crystallization and moisture infiltration [15], while conservation experts warn that unchecked degradation could ultimately lead to partial collapse in structurally weakened zones [16,17]. Such risks echo global cases where heritage monuments suffered irreversible losses in the absence of proper digital records, underscoring the urgent need to preserve what remains.

Prior documentation of the Saqqara pyramids has relied predominantly on traditional archaeological survey methods, manual architectural drawings, and published excavation records accumulated over more than a century of scholarly investigation [8]. For the Step Pyramid of Djoser, foundational architectural records were established through long-term French archaeological missions [8], while the pyramids of Unas, Teti, and Userkaf have been documented primarily through excavation reports providing plan dimensions and structural descriptions [9]. These records, although invaluable as archaeological references, are limited to 2D representations of incomplete or partially reconstructed structural forms and do not provide georeferenced, three-dimensional spatial data suitable for quantitative deformation analysis, volumetric assessment, or long-term digital monitoring. More recent international research programmers, including those documented in Staring [9] and Myśliwiec [10], have significantly advanced the understanding of the site's architectural development and historical stratigraphy, yet high-resolution 3D metric documentation of the pyramid structures themselves remains absent from the literature.

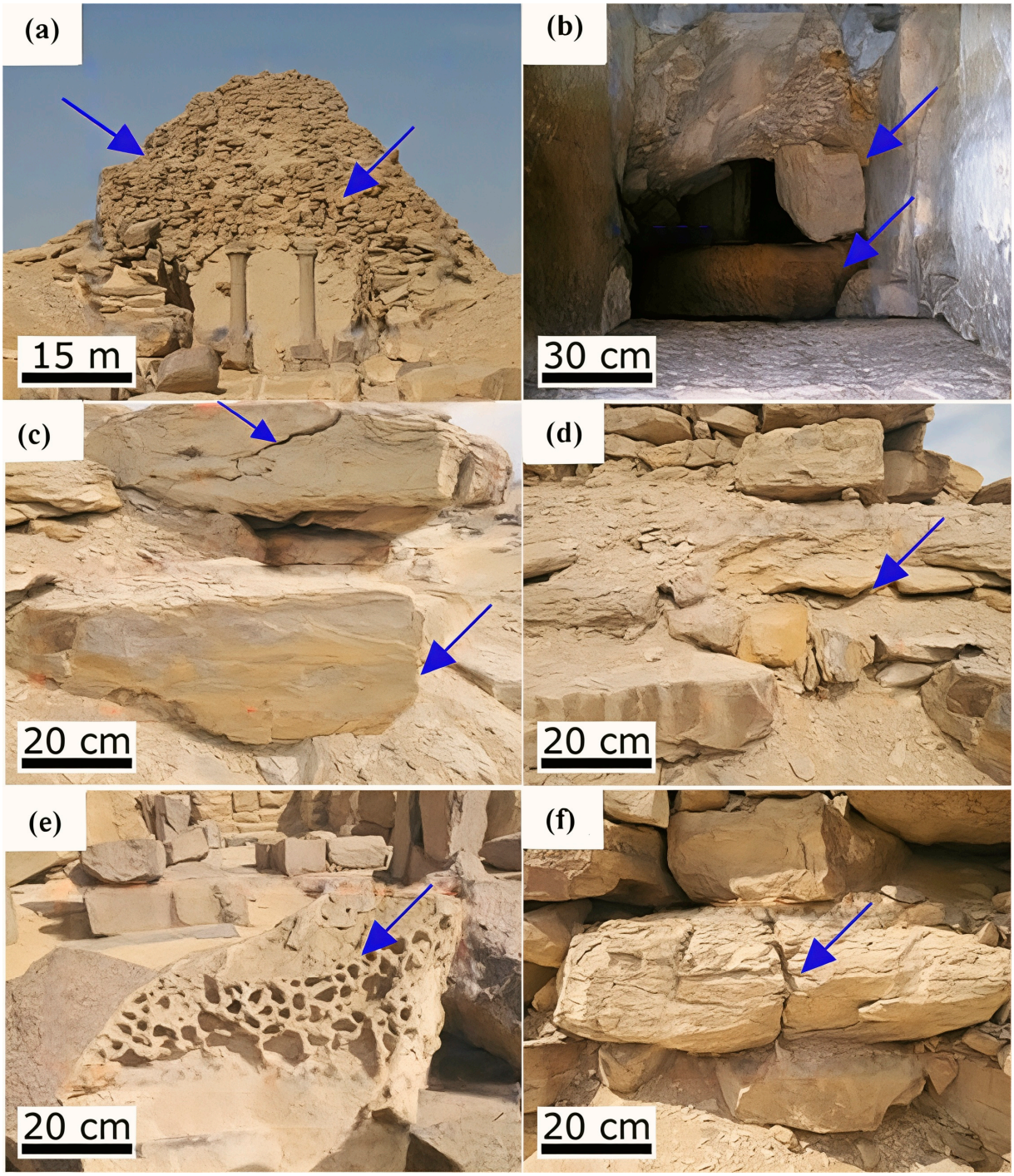

Figure 2. Examples of damage and deterioration in the Userkaf pyramid: (**a**) failure of core and casing stone blocks due to earthquakes and environmental shifts (blue arrow), (**b**) structural cracks and disintegration from seismic activity (blue arrow), (**c**) spalling and separation of stone blocks (blue arrow), (**d**) scaling, powdering, and irregular weathering of sandy limestone (blue arrow), (**e**) alveolar weathering (blue arrow), and (**f**) splitting in stone blocks (blue arrow).

Traditional documentation techniques, such as manual drawings, 2D photography, or basic survey tools, are insufficient to capture the three-dimensional complexity, current condition, and spatial relationships among these monuments [18]. There is an urgent need for modern digital documentation techniques that are non-invasive, highly accurate, scalable, and capable of long-term monitoring [19,20]. Among available tools, Terrestrial Laser Scanning (TLS) provides very high spatial resolution and reliability for architectural-scale

documentation. While oblique-view photogrammetry has proven effective in capturing complex geometries and overcoming some limitations of traditional aerial photogrammetry [21], TLS excels in recording vertical and irregular surfaces, detailed reliefs, and large-scale stone blocks with sub-centimeter precision [22]. These capabilities make it especially valuable for Saqqara, where surface textures, structural deformations, and intricate masonry details require preservation with geometric accuracy.

The primary aim of this study is to digitally document four key pyramids at Saqqara, Djoser, Unas, Teti, and Userkaf, using TLS technology integrated with precise geodetic control based on GNSS and Total Station networks. This research is designed to address critical documentation gaps by producing high-resolution, georeferenced point-cloud models and derived 3D products, such as mesh models and contour maps, which serve as both scientific datasets and conservation resources.

Building on this foundation, the study moves beyond conventional TLS applications by establishing a high-precision, georeferenced, and analysis-ready digital baseline for these monuments. Through the integration of multi-sensor geomatics and large-scale TLS datasets, it provides quantitative and reproducible metrics of structural degradation, deformation, and volumetric loss with unprecedented accuracy. These results not only refine the current understanding of the preservation state of the studied pyramids but also highlight the critical role of geodetically controlled 3D documentation as a basis for long-term monitoring, risk assessment, and evidence-based conservation planning. Consequently, the proposed framework represents a transferable approach for safeguarding complex archaeological sites, particularly those inscribed on the UNESCO World Heritage List and exposed to ongoing environmental and anthropogenic pressures.

This study builds on global precedents where TLS has proven effective in safeguarding endangered heritage sites, such as Machu Picchu [23], Petra [24], and the Roman Forum [25]. By applying similar techniques to the Saqqara pyramids, arguably one of the most archaeologically and architecturally diverse sites in Egypt, this research contributes to the broader international effort in digital heritage preservation and demonstrates how modern geomatics can bridge scientific inquiry and conservation practice in one of the world's most culturally significant regions.

2. Methodology and Workflow

The following sections describe the integrated geomatics methodology developed to produce these findings, beginning with the principles and instrumentation of TLS.

2.1. Terrestrial Laser Scanning (TLS)

The TLS is an active, non-contact remote sensing technique that rapidly acquires dense three-dimensional point clouds representing the surface geometry of scanned objects or environments. TLS systems function by emitting laser pulses that reflect off surfaces and return to the scanner, where the time-of-flight or phase shift is measured in conjunction with the angular orientation of the scanner's rotating head. These measurements are then used to compute the spatial coordinates (X, Y, Z) of the measured points relative to the scanner's position [26,27]. Its millimeter-to-centimeter accuracy, non-invasive operation, and capacity to capture comprehensive surface geometry make it particularly effective for documenting complex heritage structures such as the Saqqara pyramids, where surface textures, structural deformations, and intricate masonry details require preservation with geometric precision [28,29].

2.2. Instrumentation

The scanning campaign was conducted using an integrated geomatics approach that combined TLS, Total Station measurements, and GNSS technologies to ensure robust georeferencing. A Trimble TX6 phase-based terrestrial laser scanner (Trimble Inc., Sunnyvale, CA, USA) was utilized during the campaign (Table 1) [30,31].

Table 1. Technical specifications of the Trimble TX6 terrestrial laser scanner employed for high precision documentation of archaeological structures at Saqqara. This table summarizes the core performance parameters including Scanning Speed, accuracy, field of view, and integrated imaging technology.

Characteristic	Specification
Scanner Type	Phase-based 3D Terrestrial Laser Scanner
Technology	Trimble Lightning technology (phase-shift measurement)
Maximum Range	80 m (standard), up to 120 m (extended mode)
Scanning Speed	Up to 500,000 points per second
Distance Accuracy	±2 mm
Angular Accuracy	Horizontal: 25 µrad (0.0014°) Vertical: 25 µrad (0.0014°)
Field of View (FOV)	360° (horizontal) × 317° (vertical)
Resolution	Adjustable (standard scans 6.3 mm at 10 m; high resolution <3 mm at 10 m)
Integrated Camera	High Dynamic Range (HDR) panoramic camera (color imagery)
Scan Time per Station	~10–15 min (site-dependent)
Protection Class	IP54 (dust- and splash-resistant)
Operating Temperature	−10 °C to +50 °C
Weight	Approx. 11.5 kg (including battery)
Data Output Formats	Compatible with Trimble RealWorks, E57, LAZ, PTS, PTX, etc.
Positioning and Integration	Integrated with GNSS and Total Station control points (for georeferencing)

For high-accuracy measurement of ground control points (GCPs) and reference targets, a Trimble M3 DR5 Total Station (Trimble Inc., Sunnyvale, CA, USA) was employed. This instrument features a 5″ angular accuracy (DIN 18723), an EDM distance accuracy of ±(3 + 2 ppm × D) mm in prism mode, and a reflectorless measurement range of up to 300 m (under good conditions), making it well suited for precise target coordination and control network densification in open archaeological environments. Additionally, Trimble R8 dual-frequency GNSS receivers (Trimble Inc., Sunnyvale, CA, USA) were used to establish the primary geodetic control network. The R8 supports GPS L1/L2, L2C, L5 and GLONASS L1/L2 signals via Trimble R-Track technology, delivering static/fast-static positioning accuracy of ±5 mm + 0.5 ppm RMS (horizontal) and ±5 mm + 1 ppm RMS (vertical). By employing static and rapid-static survey techniques, the system delivered accurate coordinates referenced to the WGS84/UTM coordinate system, ensuring spatial consistency across all collected datasets [30,32].

The Trimble TX6 TLS was verified in accordance with the simplified field test procedure of ISO 17123-9:2018, which evaluates scanner precision through repeated measurements of targets at defined distances [33]. The scanner was factory-serviced, and its calibration certificate confirmed current. A pre-field functional check was performed by scanning a set of flat checkerboard reference targets positioned at known distances of 10 m, 30 m, and 50 m from the scanner. The 3D coordinates of each target center were extracted from the point cloud and compared against the Total Station-measured reference

coordinates. Point-to-target residuals were computed as the 3D Euclidean distance between the scanner-derived and reference positions, and all residuals were confirmed within the manufacturer-specified ±2 mm distance accuracy. The scanner's internal self-levelling and tilt-compensation system was verified at each setup using the onboard electronic level.

The Trimble M3 DR5 Total Station was verified in accordance with the simplified field test procedure of ISO 17123-5:2018, which evaluates total station precision through coordinate measurements in a test field without nominal values [34]. Prior to first use, the following checks were performed: (i) horizontal collimation error was determined by measuring the same target in face-left and face-right configurations and computing the difference in horizontal circle readings the mean of the two face readings eliminates this error in subsequent measurements; (ii) vertical index error (trunnion axis error) was determined by face-left and face-right measurements of the same target's zenith angle, with corrections applied where necessary; (iii) the circular bubble and electronic tilt sensor were verified and adjusted. Additionally, the EDM precision was checked by measuring a baseline of known length, with the result compared against the reference value.

The Trimble R8 GNSS receivers were verified prior to field deployment in accordance with the verification principles of ISO 17123-11:2025, which specifies field procedures for GNSS-based coordinate determination [35]. Each receiver was tested by occupying the NRIAG geodetic benchmark, a point of known coordinates established in the national geodetic reference frame, in static observation mode for a 30 min session, and the derived coordinates were compared against the reference values. Positional discrepancies in horizontal and vertical components were found to be within the manufacturer-specified static accuracy. PDOP values were monitored throughout all sessions and maintained below 3.0.

2.3. Field Procedure and Scan Strategy

Prior to scanning, a detailed survey plan was prepared to optimize station locations and maximize surface coverage. Each pyramid was scanned from multiple viewpoints with a minimum of 30–40% overlap between scans to ensure robust registration. The scanner's resolution was adjusted according to structural complexity and areas of visible deterioration. Special attention was given to minimizing occlusions by positioning the scanner on elevated points, stable observation platforms, and within accessible spaces [36]. Flat black-and-white targets were placed across the site to aid automatic and manual scan registration (Figure 3).

2.4. Geodetic Control Network

A foundational element of this project was the establishment of a high-precision geodetic control network to ensure absolute spatial accuracy across the entire study area. The network was designed in two hierarchical tiers: a primary network of four GCPs established by static GNSS, subsequently densified by a secondary network of approximately 32 points measured with the Trimble M3 DR5 Total Station [37].

2.4.1. GNSS Survey Planning and Satellite Availability Analysis

Prior to fieldwork, a GNSS mission planning analysis was conducted to identify optimal observation windows at the Saqqara site (latitude ~29.87°N, longitude ~31.21°E). Observation windows were selected to coincide with periods of favorable satellite geometry, defined as PDOP values consistently below 3 and a minimum of six simultaneously tracked satellites from combined GPS and GLONASS constellations. An elevation mask angle of 15° was applied during both planning and observation to reduce the influence of low-elevation multipath signals. The four GCP locations were additionally assessed for local obstructions using a horizon obstruction diagram prepared during site reconnaissance, confirming unobstructed sky views above the 15° mask angle at all selected monument positions.

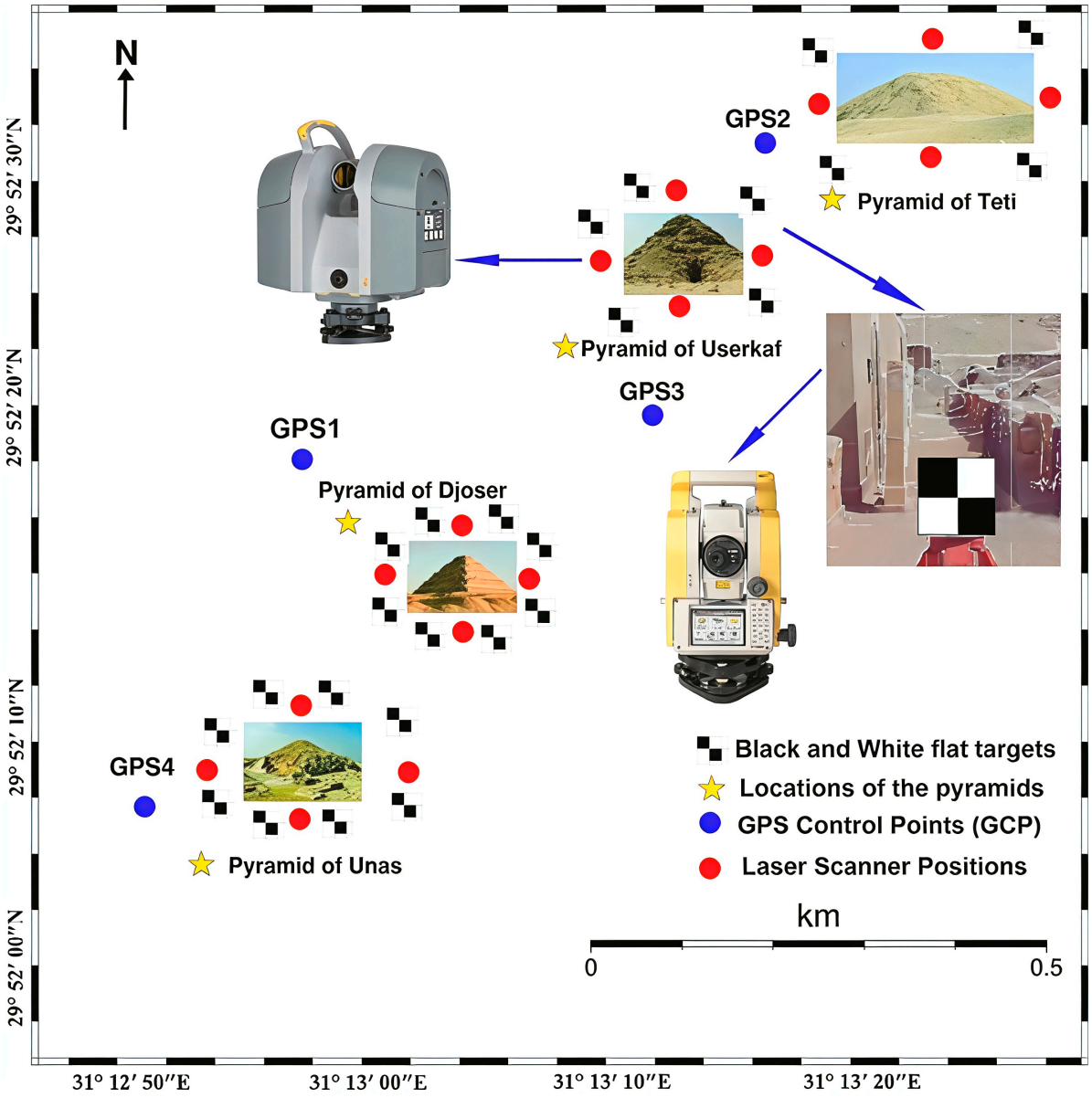

Figure 3. Spatial layout of the TLS survey at the Saqqara pyramids, integrating the established geodetic control network with the corresponding scanning configuration. The figure depicts the four primary geodetic GCPs distributed around the pyramid zones, the numbered TLS scanner station positions surrounding each pyramid, and the Trimble TX6 phase-based laser scanner used for data acquisition. Control targets are shown in strategically selected locations to maximize coverage, reduce occlusions, and enable precise registration of multi-view scans. Total Station setup positions are indicated as well, used in conjunction with GNSS data for densifying the control network and ensuring accurate georeferencing of all TLS datasets.

To ensure long-term physical preservation and future revisit ability, each primary GCP was monumented as a permanent reinforced concrete ground mark cast to a depth of approximately 0.5 m, with a stainless-steel centering bolt embedded at the surface for precise forced-centering. Each monument was inscribed with its point identifier and survey year, photographed, and described in a detailed recovery sheet referencing permanent nearby features. All coordinate descriptions and recovery sketches are archived at NRIAG and are available to future survey teams, ensuring that the georeferenced baseline established by this study can be precisely re-occupied for future deformation monitoring and change detection campaigns.

2.4.2. Reference Station and Receiver Configuration

The geodetic reference frame for the entire control network was anchored to an Egyptian Survey Authority (ESA) continuously operating reference station (CORS), designated REF, with the following established coordinates referenced to WGS84/UTM Zone 36N with coordinate accuracy ±1 mm (H), ±4 mm (V).

The REF station coordinates were adopted directly from the official ESA geodetic database and held fixed as the constraint in all baseline processing and network adjustment, ensuring that the entire survey is tied to the national geodetic reference frame of Egypt and is consistent with WGS84. Five Trimble R8 dual-frequency GNSS receivers were deployed simultaneously: the REF station served as the fixed reference, while the other receivers occupied each of the four GCP monuments. Each receiver was mounted on a fixed-height tripod with tribrach and optical plummet; antenna heights were measured using a calibrated slant-height rod and reduced to the antenna reference point using manufacturer-provided phase center offsets.

2.4.3. Observation Parameters and Session Duration

All GNSS observations were recorded at a 5 s logging interval to the receivers' internal memory in Trimble. T02 raw data format, capturing both GPS (L1/L2/L2C/L5) and GLONASS (L1/L2) signals. Each GCP was observed in a continuous static session of four days, which at the baseline lengths involved is well in excess of the duration required for reliable carrier-phase ambiguity resolution and sub-centimeter positioning. Three observation sessions were conducted with the REF station remaining stationary and continuously recording throughout all sessions to provide a common baseline origin. The resulting observation dataset comprised four independent baselines connecting REF to each of GPS1, GPS2, GPS3, and GPS4. Table 2 summarizes the key observation parameters applied uniformly across all sessions.

Table 2. Summary of GNSS observation parameters applied during primary control network establishment at Saqqara.

Parameter	Value
Observation mode	Static differential baseline
GNSS constellations tracked	GPS (L1/L2/L2C/L5) + GLONASS (L1/L2)
Elevation mask angle	15°
Recording interval	5 s
Minimum session duration	4 Days
Minimum satellites tracked	6 (GPS + GLONASS combined)
Maximum PDOP	<3
Reference station	REF (ESA CORS, fixed constraint)

2.4.4. GNSS Data Processing and Atmospheric Corrections

Raw GNSS observations were post-processed using TBC software (v5.2, Trimble Inc., Sunnyvale, CA, USA) with integer ambiguity resolution enabled. The ionosphere-free linear combination (L3) was applied during baseline processing to eliminate the first-order ionospheric delay, which is the dominant atmospheric error source at the baseline lengths and observation durations used in this study [38]. The Saastamoinen tropospheric model was applied to correct for dry and wet tropospheric delay, using surface meteorological observations of temperature, pressure, and relative humidity recorded at the site during each session. Final precise ephemeris products from the International GNSS Service (IGS) were

used in preference to broadcast ephemerides, providing satellite orbit and clock corrections at the sub-centimeter level and eliminating satellite ephemeris error as a significant error source [39]. Fixed integer ambiguity solutions were sought for all baselines, with a baseline accepted only when TBC reported a fixed solution with a ratio test value greater than 2.0, confirming reliable ambiguity resolution; all four baselines achieved fixed solutions on the first observation attempt [39]. All baseline quality indicators, including carrier-phase residuals below 3 mm, reference variance, and fixed/float ratio, were confirmed within acceptance thresholds.

2.4.5. Network Adjustment and Accuracy Assessment

Following baseline processing, a constrained least-squares network adjustment was performed in TBC, with the REF station coordinates provided by the Egyptian Survey Authority held fixed as the single constraint. The four GCP coordinates were estimated as free parameters, with the adjustment optimally distributing observational residuals across all baselines. Closure checks were performed by computing the misclosures of all possible closed loops formed by the four baselines. All loop misclosures were found to be below 7 mm in all three coordinate components, confirming internal network consistency and the absence of gross errors. These values are consistent with the static performance specification of the Trimble R8 receiver and confirm that the network accuracy is well within the ±0.5 mm to ±1 cm overall georeferencing target of the study. The final adjusted GCP coordinates are listed in Table 3.

Table 3. Adjusted geodetic control network coordinates for the ESA reference station (REF) and the four primary GCPs established across the Saqqara pyramid zones. Coordinates are expressed in the UTM Zone 36N projected system, referenced to WGS84, with Easting and Northing values given to millimeter precision. Ellipsoidal heights are referenced to the WGS84 ellipsoid. Standard deviations (σE, σN, σH) are derived from the constrained least-squares network adjustment performed using TBC software.

Point ID	Easting (m)	Northing (m)	Ellipsoidal Height (m)	σE (mm)	σN (mm)	σH (mm)
REF (ESA)	327,791.812	3,306,859.282	47.187	±1	±1	±4
GPS1	327,857.087	3,306,262.841	68.928	±3	±4	±5
GPS2	327,582.021	3,306,041.723	73.371	±4	±3	±7
GPS3	327,688.795	3,305,591.995	70.508	±3	±2	±6
GPS4	327,430.711	3,305,217.091	74.397	±3	±4	±7

2.4.6. Total Station Densification

The primary GNSS network was densified using the Trimble M3 DR5 Total Station to establish 32 secondary control points and scan registration targets across all four pyramid zones. Densification was necessary to reduce the effective control spacing from ~300–500 m (primary GNSS GCP spacing) to ~15–20 m around each pyramid face, providing direct geometric constraints for TLS scan registration. Standard Trimble 6.25 cm prisms on fixed-height poles were used for prism-mode observations; scan registration targets were measured in reflectorless EDM mode to eliminate prism-centering error.

The densification employed free stationing (resection) combined with forward radiation and, where geometry permitted, forward intersection. For each instrument setup, the Total Station was positioned at a freely chosen station with simultaneous visibility of at least three primary GCPs or previously established secondary points, and its coordinates were determined by free-stationing resection. Secondary control points and scan registration targets were then measured by radiation from that station. Critically, most targets

were deliberately placed to be visible from at least two independent instrument setups, enabling their coordinates to be determined by forward intersection with geometric redundancy rather than by single-station radiation alone. All angular observations were made in face-left and face-right configurations; mean values were used to eliminate horizontal collimation and vertical index errors. Atmospheric corrections were applied to all EDM observations [40].

The GNSS and Total Station observations were adjusted in two sequential stages [41,42]: first, the GNSS baseline network was adjusted with the REF station held fixed, yielding GPS1–GPS4 coordinates (Table 3); second, all Total Station observations were adjusted in a constrained terrestrial least-squares adjustment within TBC with the GNSS GCP coordinates held fixed. This approach propagates GNSS network accuracy into the local densification while exploiting the full redundancy of the terrestrial observation network. The achieved accuracy of secondary points was better than ±5 mm planimetric and ±8 mm in height, with free-stationing resection RMS residuals below 3 mm and 5″ across all instrument stations.

To provide full transparency of the densification network geometry, Table A1 in Appendix A presents the UTM Zone 36N coordinates of all 32 Total Station-derived secondary control points, grouped by pyramid zone. The spatial distribution of these points, eight per pyramid, was designed with points placed at 15–25 m from each pyramid face at cardinal and inter-cardinal positions.

The formal accuracy of the secondary control points and scan registration targets, as derived from the constrained terrestrial least-squares adjustment in TBC, is summarized in Table 4. The achieved positional accuracy of the secondary points was better than ±5 mm in planimetry and ±8 mm in height for all 32 points, confirming that the densified network meets the sub-centimeter accuracy requirement for TLS scan registration. The mean residuals of the free stationing resections, computed as the RMS of the differences between the observed and back-calculated distances and directions to the known control points, were below 3 mm and 5″, respectively, across all instrument stations, confirming the internal consistency of the terrestrial observations and the absence of gross errors.

Table 4. Summary of Total Station densification network accuracy assessment, derived from the constrained least-squares adjustment in TBC.

Quality Metric	Achieved Value
Number of secondary points established	32
Measurement methodology	Free stationing (resection) + radiation
Minimum known points per resection	3
Mean resection RMS (distance residuals)	<3 mm
Mean resection RMS (angular residuals)	<5″
Max. σ planimetric (secondary points)	±5 mm
Max. σ height (secondary points)	±8 mm
Adjustment type	Constrained least-squares (GNSS GCPs fixed)
Processing software	TBC
Min. control targets per TLS scan station	2

2.5. Workflow

The adopted workflow aligns with best practices established in international heritage scanning projects, such as the 3D documentation of Machu Picchu [23], Petra [24], and the Roman Forum [25]. These precedents validate terrestrial laser scanning integrated with

geodetic control as a robust method for capturing complex architectural heritage with high fidelity. The workflow in this study follows a refined geomatics approach, consisting of five phases designed to produce high-fidelity, georeferenced 3D models of the pyramids (Figure 4).

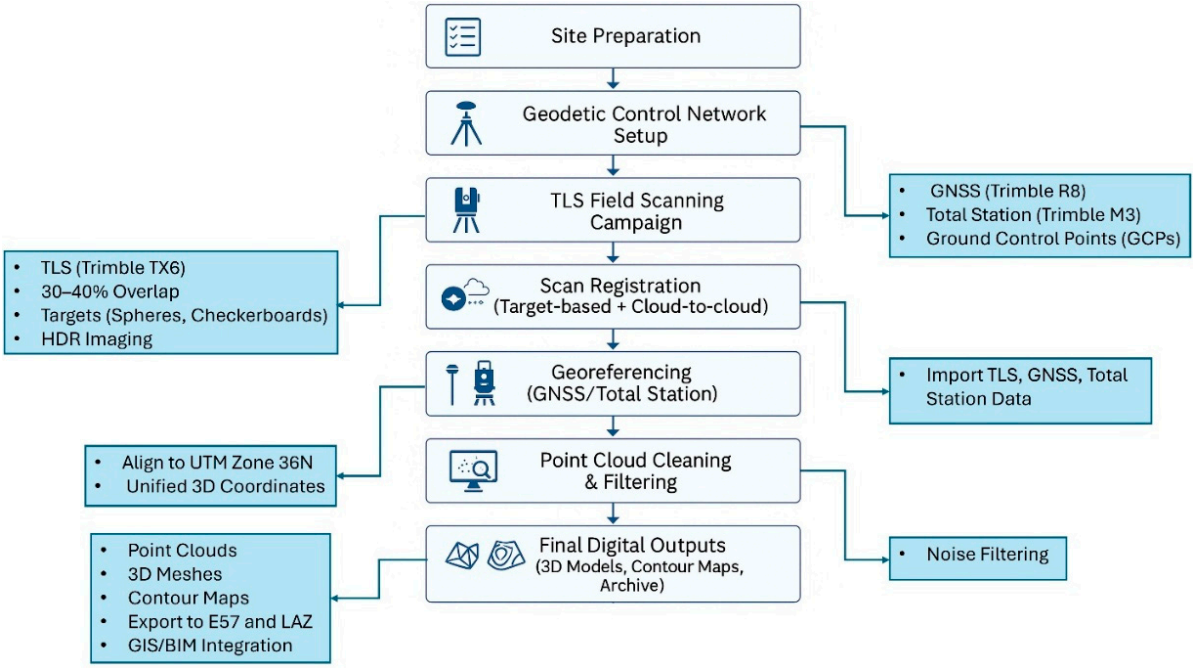

Figure 4. Workflow for 3D documentation of the Saqqara pyramids.

3. Data Acquisition

The field campaign was conducted on four significant pyramid structures in the Saqqara archaeological zone: Unas, Djoser (Step Pyramid), Userkaf, and Teti. The primary objective was to capture the external geometry of these monuments using a systematic TLS approach to ensure high geometric fidelity and complete spatial coverage.

3.1. Planning and Geodetic Control

Prior to data acquisition, a comprehensive site reconnaissance was undertaken to determine optimal scanning positions. Locations were chosen to provide maximum visibility of pyramid faces while minimizing occlusions from terrain irregularities, adjacent structures, or modern installations. Each scan station was selected to maintain sufficient overlap between scans, supporting robust cloud registration [43,44]. The spatial referencing of the project relied on a high-precision geodetic control network comprising four GCPs established using Trimble R8 GNSS receivers. This network was further densified with a Trimble M3 DR5 Total Station to enhance positional accuracy.

3.2. Laser Scanning Execution

At each scan station, the Trimble TX6 scanner was mounted on a stable tripod and precisely leveled. Scanning parameters such as resolution, scan speed, and angular field of view were adjusted according to scanning distance and architectural complexity [45]. Standardized checkerboard targets were strategically placed within the scan zone and georeferenced using the Total Station. These targets acted as tie points for accurate multi-scan registration. The TLS system captured a large number of points per scan, along with high-resolution HDR imagery from its integrated camera [46,47], later used for point cloud colorization.

At each station, immediate visual and metric checks ensured scan completeness before moving to the next position. This workflow was repeated for all four pyramids, producing 16 scan stations containing millions of data points. In total, 16 high-resolution scan positions were distributed across the pyramid zones. All pyramid scans were conducted at Level 3 resolution of the TLS TX6, with each scan requiring approximately 21 min (Figure 5). The scan station positions were deliberately planned in relation to the physical dimensions and current preservation state of each pyramid, with scanning distances adjusted to ensure full surface coverage within the effective range of the Trimble TX6 while maintaining the required point density for sub-centimeter documentation. Table 5 summarizes the key acquisition parameters for each pyramid, including station configuration, average scanning distances derived from the pyramid base dimensions, target distribution, and approximate point cloud yield.

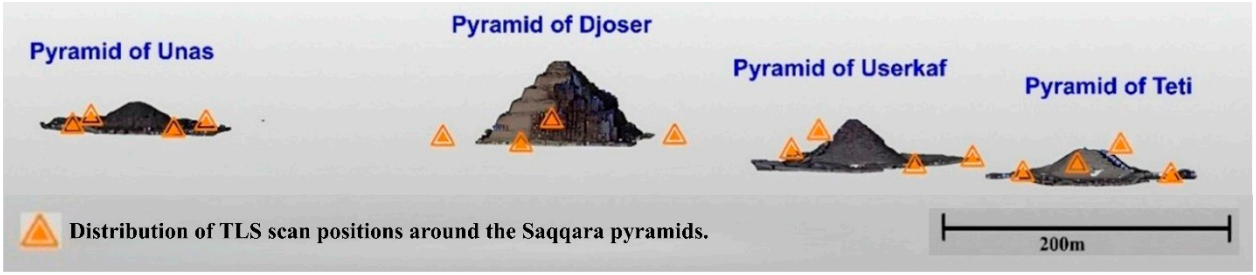

Figure 5. Distribution of selected TLS stations around the four Saqqara pyramids (Unas, Djoser, Userkaf, and Teti), with four scan stations positioned around each pyramid to ensure comprehensive surface coverage.

Table 5. Summary of TLS acquisition parameters for each pyramid at Saqqara, derived from the survey configuration and pyramid dimensions documented in the manuscript.

Parameter	Djoser	Unas	Teti	Userkaf
Current height (m)	~57	~20	~18	~18
Approximate base dimensions (m)	~125 × 109	~57 × 57	~78 × 78	~73 × 73
Number of scan stations	4	4	4	4
Station distribution	Cardinal azimuths	Cardinal azimuths	Cardinal azimuths	Cardinal azimuths
Average scanning distance (m)	~50–80	~25–40	~35–50	~30–45
Maximum scanning distance (m)	~80	~50	~60	~55
Number of registration targets placed	8	8	8	8
Min. targets visible per station	2	2	2	2
Scan resolution level	TX6 Level 3	TX6 Level 3	TX6 Level 3	TX6 Level 3
Approx. scan time per station (min)	~21	~21	~21	~21
Scan overlap between adjacent stations	30–40%	30–40%	30–40%	30–40%
Approx. points acquired (millions)	~700	~450	~500	~450

This resolution was selected because it provides higher point density and details, and the same settings were applied consistently at all scanning stations. The entire survey was completed in six days (Table 6). The acquisition process followed two steps: laser

scanning followed by image capture. The Trimble TX6 collected both geometric data (XYZ coordinates) and intensity information at each scan position. The intensity value represents the ratio of returned to emitted laser signal power, governed by the LiDAR range equation [29,48], and is primarily determined by four physical parameters: (i) surface reflectivity (albedo); (ii) angle of incidence between the laser beam and the surface normal, with intensity decreasing approximately as the cosine of this angle following Lambert's cosine law [48,49]; (iii) scanning range, with intensity decreasing as the inverse square of distance; and (iv) surface roughness at the laser footprint scale, which controls whether reflection is specular or diffuse [49,50]. For the sandy nummulitic limestone of the Saqqara pyramids, these factors are particularly informative: intact stone faces produce strong, stable Lambertian returns, while weathered, salt-encrusted, or biologically colonized surfaces exhibit measurably reduced reflectivity due to changes in surface chemistry and microstructure [50]. Surfaces affected by spalling, alveolar weathering, or cracking generate locally variable intensity patterns due to oblique micro-incidence geometry, and at high incidence angles, common when scanning collapsed block piles, non-Lambertian behavior becomes significant [49,51]. These physical relationships mean that the intensity dataset encodes surface material properties alongside geometry, enabling distinction between intact limestone, weathered zones, salt-affected surfaces, and debris accumulations through their characteristic intensity signatures [50,51].

Table 6. Summary of fieldwork and office tasks for 3D model generation of the Saqqara pyramids, detailing phases, involved personnel, and total labor time.

Phase	Task	Team	Required Time
Planning Phase	Site reconnaissance, scan station plan, geodetic network design, safety and access planning	1 researcher and 1 survey engineer (2 persons)	5 working days total ($2 \times 5 \times 8 = 80$ h)
Fieldwork Geodetic Control	Establish GNSS/Total Station GCPs, survey targets	1 researcher and 1 technician (2 persons)	6 working days total ($2 \times 6 \times 8 = 96$ h)
Fieldwork TLS Acquisition	Trimble TX6 scanning (16 stations total across 4 pyramids), target placement, HDR imagery, daily calibration and backups	2 researchers and 1 technician (3 persons)	4 working days total ($3 \times 4 \times 8 = 96$ h)
Office GNSS/TS Processing	Process GNSS static/rapid-static results and produce control coordinates	1 geodesist (1 person)	4 working days total ($1 \times 4 \times 8 = 32$ h)
Office TLS Registration and Cleaning	Import scans to Trimble RealWorks, target-based + cloud-to-cloud registration, noise filtering and quality checks	1 TLS specialist and 2 researchers (3 persons)	6 working days total ($3 \times 6 \times 8 = 144$ h)
Office 3D Modeling and Derivatives	Mesh generation, orthophoto generation and DEM/contour extraction	1 3D modeler and 1 GIS specialist (2 persons)	3 working days total ($2 \times 3 \times 8 = 48$ h)
Office Deliverables and Archiving	Prepare E57/LAZ exports, metadata, GIS/BIM packaging and final reporting	1 researcher (1 person)	5 working days total ($1 \times 5 \times 8 = 40$ h)

4. Data Processing

After fieldwork, raw data were processed using Trimble RealWorks for TLS management and TBC for geodetic integration, producing accurate point clouds for archaeological analysis and documentation. The first stage of processing involved importing the raw TLS

scan files (TZF format from the Trimble TX6), GNSS-based control coordinates (T02 format) and Total Station measurement data (.text format) into the processing environment. A preliminary quality check was carried out to verify the completeness of the dataset and to confirm that the required number of reference targets had been recorded for each pyramid. For the Pyramid of Djoser, eight targets were acquired with a Root Mean Squared Error (RMSE) of 2.97 mm; the Pyramid of Unas was documented with eight targets and a mean RMSE of 2.96 mm; the Pyramid of Teti with eight targets and a RMSE of 2.98 mm; and the Pyramid of Userkaf with eight targets and a RMSE of 2.89 mm (Figure 6a). In the context of TLS target-based registration, two distinct error metrics are reported for each reference target [26]. The fitting error (σ_fit) characterizes the precision of target center detection within a single scan, computed as the RMS of distances between laser points on the target surface and the best-fit geometric model:

$$\sigma_{\{fit\}} = \sqrt{\left\{ \frac{1}{n} \sum_{\{i=1\}}^{\{n\} d_i^2} d_i^2 \right\}}$$

where n is the number of points measured on the target and d_i^2 is the perpendicular distance from the i-th point to the fitted plane. It is primarily influenced by point density, laser spot size, surface reflectivity, and angle of incidence. The residual error (σ_res) characterizes the 3D positional discrepancy between the Total Station-measured coordinates of a target and its registered position in the aligned point cloud after transformation:

$$\sigma_{res} = \sqrt{\Delta X^2 + \Delta Y^2 + \Delta Z^2}$$

where ΔX, ΔY, and ΔZ are the coordinate differences between Total Station-determined and TLS-registered target positions. The residual error integrates contributions from fitting error, target placement uncertainty, and Total Station measurement accuracy. The relationship between these two metrics is examined in Figure 6b to assess the internal consistency of the registration solution for each pyramid.

To investigate measurement consistency, the correlation between fitting and residual errors was analyzed (Figure 6b). The analysis shows that while Djoser and Teti exhibit moderate positive correlations, Userkaf displays a more clustered pattern, indicating greater measurement consistency for that pyramid.

These RMSE values represent direct outputs of the Trimble RealWorks registration algorithm, computed from the residuals of eight independently measured targets per pyramid. The values consistently fall in the range of 2.89–2.98 mm, which is physically consistent with the TX6 instrument distance accuracy of ±2 mm. The overall registration error budget is expected to exceed the single-measurement noise floor due to the accumulation of target centering, angular, and atmospheric error contributions, and is in agreement with the mean residual range of 2.4–3.2 mm. These values are well within the accepted accuracy thresholds for TLS [23,52–54].

Following import, all scan positions for each pyramid were registered into a single unified point cloud. Registration was performed in two sequential stages. The first stage was target-based registration, in which common reference targets whose three-dimensional positions were independently measured using a Total Station served as the initial geometric constraints for aligning overlapping scans. The second stage involved cloud-to-cloud registration, where geometric surface features within overlapping areas were matched using the Iterative Closest Point (ICP) algorithm to minimize residual distances between point clouds. Registration accuracy was evaluated using residual errors and RMSE metrics, and only scans with alignment errors below 4 mm were retained in the final dataset. This

procedure followed established TLS documentation practices outlined in [55,56], ensuring both spatial precision and methodological consistency.

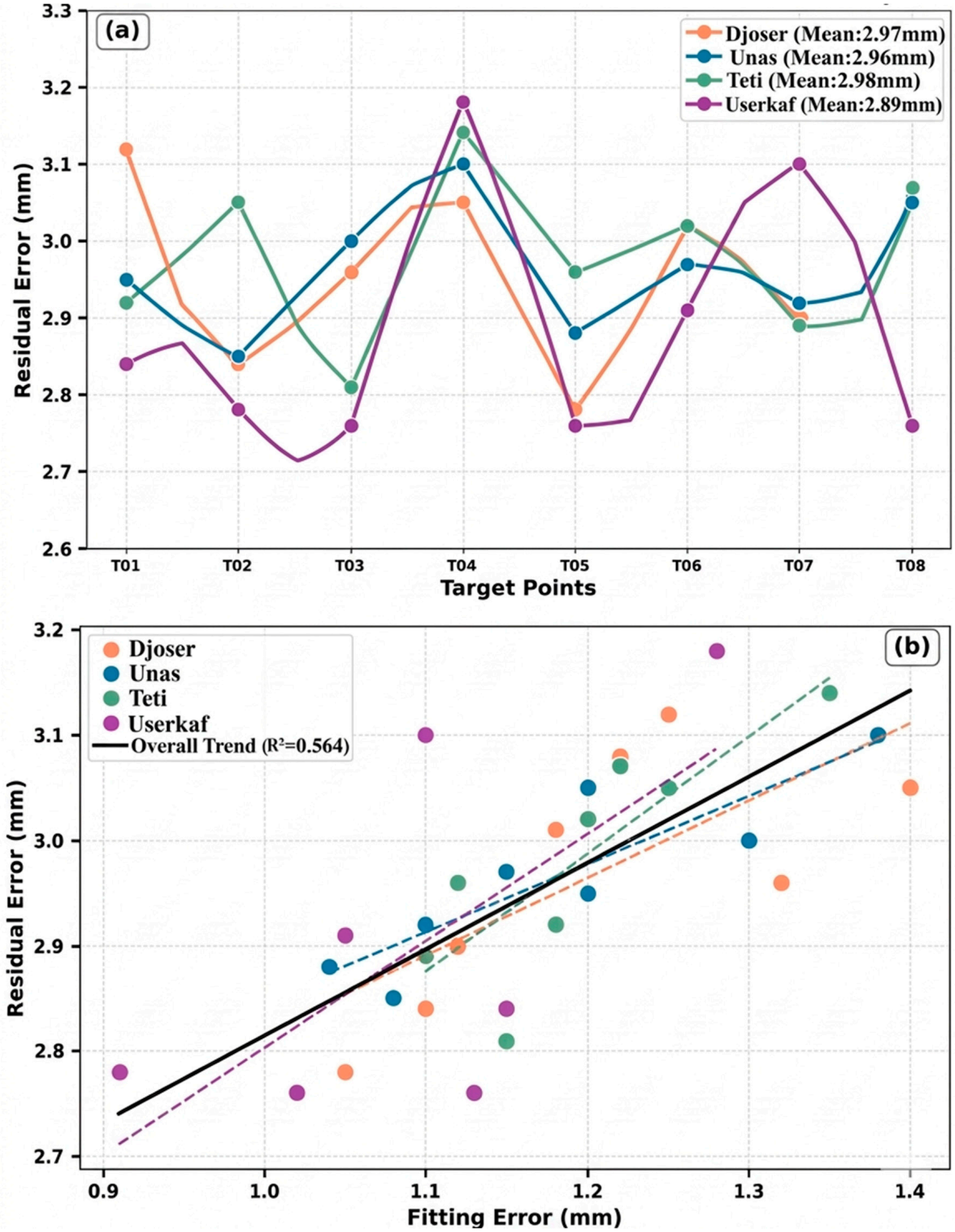

Figure 6. (**a**) A plot of registration residual errors for TLS reference targets across the Saqqara pyramids, illustrating the spatial distribution and accuracy achieved during alignment and georeferencing. Each pyramid shows closely clustered residuals around 3 mm, reflecting the high precision of multi-stage scan registration using Total Station-derived control points. (**b**) This scatter plot with individual pyramid trend lines demonstrates the relationship between fitting errors and residual errors in the 3D laser scanning process.

Once internal registration was complete, the composite point cloud for each pyramid was georeferenced to the UTM coordinate system, Zone 36N, using GNSS-derived GCPs. This transformation ensured that the outputs were spatially compatible with external GIS datasets, photogrammetric products, and other remote sensing data, while also enabling future integration into heritage monitoring programs.

Subsequently, the georeferenced point clouds were subjected to rigorous data cleaning and noise filtering. This involved both automated and manual processes to remove stray reflections, vegetation, bystanders, and other scanning artifacts, resulting in enhanced surface definition and improved model usability. Care was taken to preserve fine architectural details and surface textures, which are particularly important for archaeological interpretation and conservation planning. Finally, high-resolution HDR panoramic images, recorded by the TX6's integrated camera, were used to assign RGB values to individual 3D points. This created photorealistic point clouds that provide not only spatial data but also visual texture critical for conservation, presentation, and virtual interpretation.

To assess the overall spatial accuracy of the final georeferenced point cloud models, a combined accuracy budget was computed by propagating the individual uncertainty components through the full processing chain. The primary GNSS control network contributed a mean horizontal standard deviation of ± 4 mm and vertical standard deviation of ± 7 mm. The Total Station densification introduced an additional planimetric uncertainty of ± 5 mm and height uncertainty of ± 8 mm. Scan registration contributed RMSE values of 2.89–2.98 mm per pyramid. Combining these components in quadrature the standard approach for independent, uncorrelated error sources yields an estimated overall 3D positional accuracy of the georeferenced point clouds of approximately ± 10–12 mm (approximately ± 1 cm). This value is well within the ± 2 cm spatial accuracy tolerance targeted for the study, which was defined as the maximum acceptable positional uncertainty for heritage documentation at this scale and consistent with accepted thresholds in the TLS heritage literature [23,52–54,57]. This represents a conservative estimate, as the dense redundancy of the control network 4 primary GNSS GCPs and 32 Total Station-derived secondary points serving 16 scan stations across four pyramids provides strong geometric control that mitigates the accumulation of individual error contributions.

It should be noted that all Total Station-measured targets were used as registration constraints, and no independent check points were withheld for external validation. Consequently, a fully independent accuracy assessment following recognized geospatial data accuracy standards such as the ASPRS Positional Accuracy Standards for Digital Geospatial Data, the National Standard for Spatial Data Accuracy (NSSDA), or STANAG 2215 was not performed. The accuracy estimates reported in this study derived from combined error propagation should therefore be understood as internally derived quality indicators rather than externally validated accuracy statements.

5. Results

Following the comprehensive TLS campaign and subsequent data processing workflow, a high-resolution, georeferenced 3D documentation dataset was produced for the four key pyramids in the Saqqara necropolis: Djoser (Step Pyramid), Unas, Teti, and Userkaf. The results include dense point cloud models, mesh models, 2D sections and derivative visualization products, offering a geometrically precise and visually detailed digital record of each monument's current condition and architectural features.

5.1. Point Cloud Models

The core product generated from the TLS campaign was a set of dense and accurately registered point clouds for each pyramid. These models achieved millimeter-level resolu-

tion in many areas, capturing the intricate geometry of the structures. Registration reports confirmed excellent alignment with the geodetic control network, with residual errors generally below 3 mm and overall spatial accuracy estimated at ±10–12 mm through combined error propagation of control network and registration uncertainties, well within the ±2 cm tolerance established as the study accuracy target for large-scale heritage documentation at this site. In addition, registration accuracy was determined through a two-stage evaluation procedure. In the first stage, target-based registration accuracy was quantified using the residual error metric (σ_res) defined, computed for all eight independently Total Station-measured targets per pyramid after the full registration transformation was applied. The per-pyramid RMSE values were 2.97 mm (Djoser), 2.96 mm (Unas), 2.98 mm (Teti), and 2.89 mm (Userkaf), all below the 4 mm acceptance threshold applied during processing. In the second stage, the geometric consistency of the registered point clouds was independently confirmed through cloud-to-cloud ICP alignment, with mean residuals across all 16 scan stations ranging from 2.4 mm to 3.2 mm consistent with and independent of the target-based RMSE values.

The point cloud analysis of the four pyramids revealed distinct characteristics for each structure. The Djoser Step Pyramid's point cloud highlighted the complexity of its stepped architectural form, including visible displacements in several tiers and surface erosion patterns on the limestone casing, providing data that can aid future restoration assessments (Figure 7).

Similarly, the Unas Pyramid, although smaller and partially collapsed, yielded a high-fidelity point cloud that captured its remaining core and surroundings, which notably helped delineate the pyramid's original slope courses despite its degraded state (Figure 8). In contrast, the Teti Pyramid was better preserved at its base, providing an exceptionally clean scan of lower structural elements that showcased its relatively stable construction blocks and foundational alignment, allowing for a detailed digital 3D point cloud model (Figure 9).

Finally, the extensively ruined Userkaf Pyramid resulted in a fragmented but valuable point cloud; despite missing sections, the scan revealed erosion depths, irregular block distribution, and remnants of internal structures, supporting theories about its construction phases and later reuse (Figure 10). A synthesized 3D visualization was created by integrating the four pyramids' models into a single spatial environment. This comparative visualization highlights spatial relationships between the pyramids and supports regional-level planning for conservation. The consistency of scan registration was evaluated through both target-based and cloud-to-cloud alignment strategies. Mean residuals between scan stations ranged from 2.4 mm to 3.2 mm, confirming sub-centimeter registration accuracy. These values fall within accepted thresholds for heritage TLS applications, as recommended by [23,52–54].

5.2. Three-Dimensional Mesh Models

Following the creation of the 2D point cloud models, 3D mesh models were generated for each pyramid using Trimble RealWorks. The workflow involved three main stages: (1) resampling the point clouds to an optimal resolution, (2) triangulation using Poisson Surface Reconstruction and Delaunay algorithms adapted to local geometry, and (3) texture mapping with HDR imagery to produce photorealistic digital surfaces.

Resampling was essential to balance computational load with geometric fidelity. Point densities were optimized based on the structural complexity of each pyramid, ranging from 0.2 cm for Djoser and Userkaf, to 0.5 cm for Teti, and 0.3 cm for Unas (Table 7). This process preserved fine architectural features while avoiding excessive mesh file sizes.

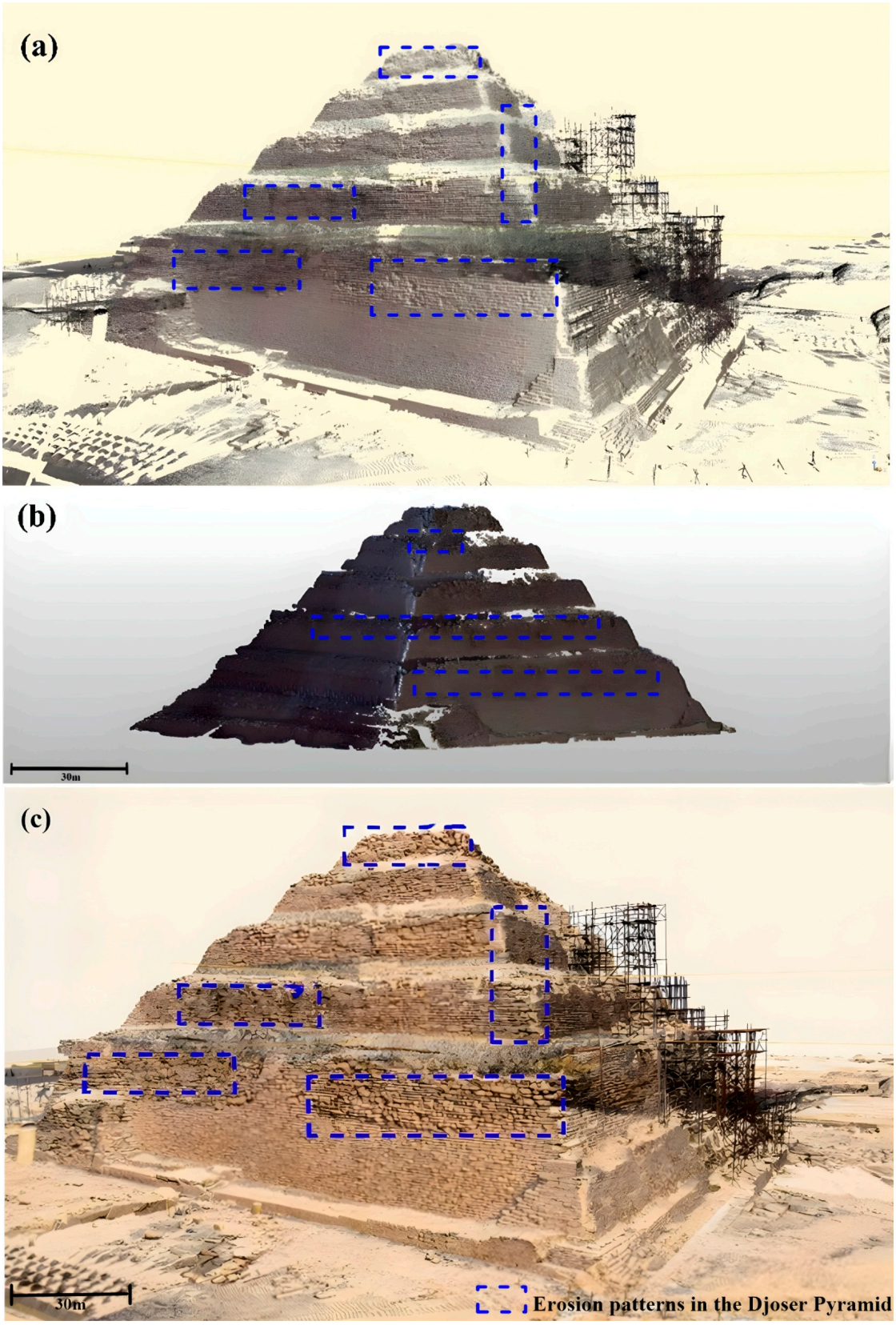

Figure 7. TLS point cloud of the Djoser Step Pyramid: (**a**). black and white geometric visualization, illustrating the structural volume and surface topography of the pyramid without color interference. (**b**) corresponding grayscale rendering highlighting geometric and structural details, including stepped tiers and erosion patterns (dashed blue line). (**c**) true color (RGB) texture visualization, integrating high-resolution HDR imagery to achieve enhanced visual realism and authentic surface detail.

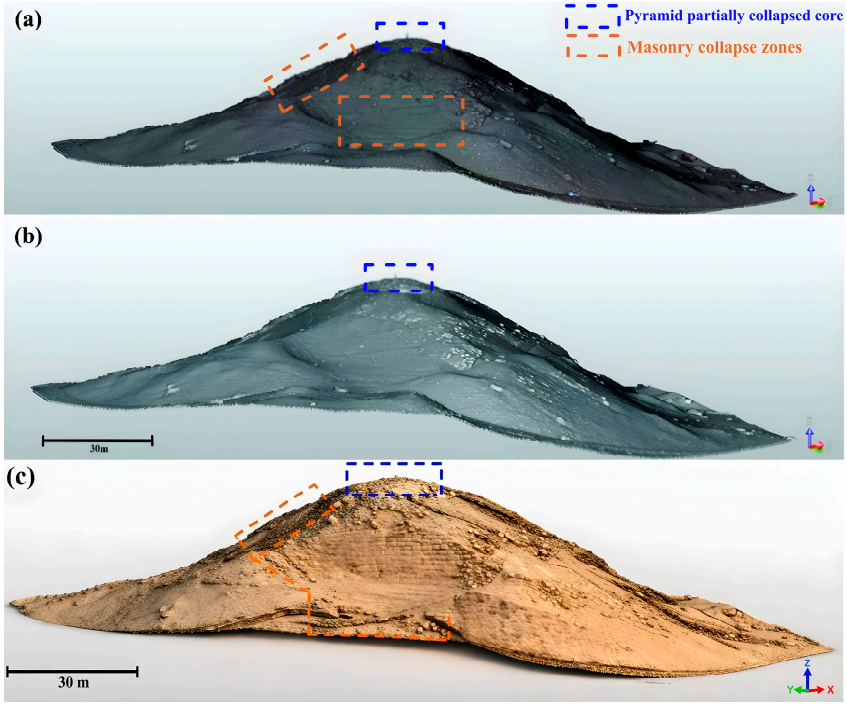

Figure 8. TLS point cloud of the Unas Pyramid: (**a**) black and white colorization, illustrating the structural volume and core geometry of the pyramid. (**b**) grayscale view emphasizing structural form despite site degradation. (**c**) True-color (RGB) mode with texture information, integrating high-resolution HDR imagery for enhanced visual realism and authentic surface detail.

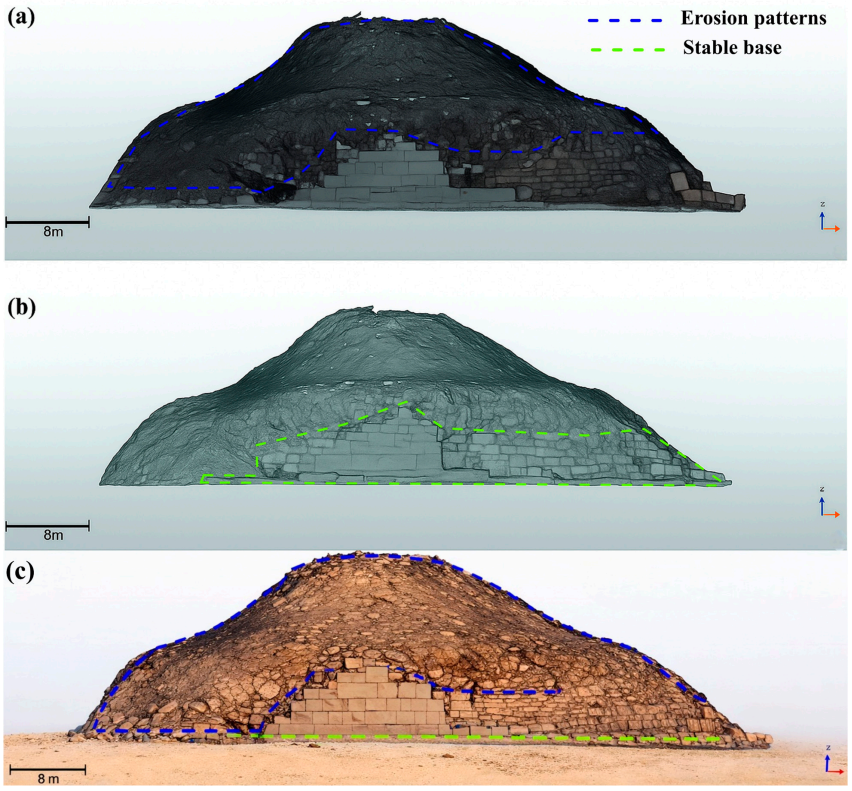

Figure 9. Point cloud model of the Teti Pyramid: (**a**) black and white colorization, highlighting the primary geometric volume and structural boundaries. (**b**) grayscale representation accentuating foundational alignment and contour variations. (**c**) True-color (RGB) mode with natural hues, integrated from high-resolution imagery to provide enhanced visual realism and authentic surface textures.

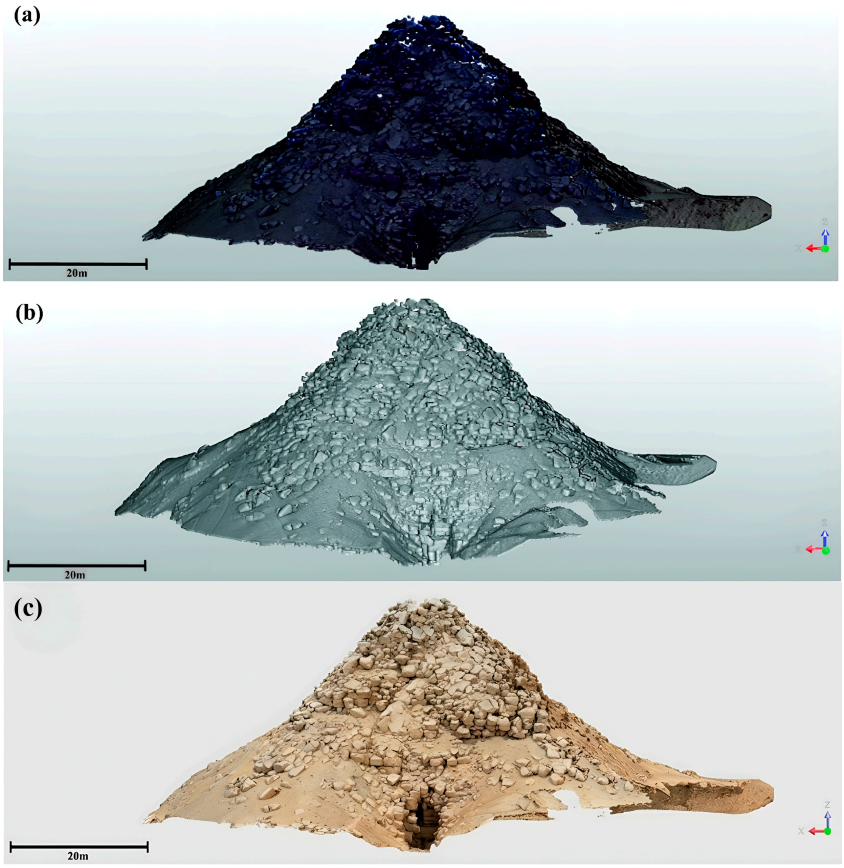

Figure 10. TLS point cloud of the Userkaf Pyramid: (**a**) black and white colorization, providing a clear geometric interpretation of the primary pyramid volume and core boundaries, (**b**) complementary grayscale model illustrating surface irregularities and fragmented conditions and (**c**) True-color (RGB) image with natural texture mapping, combining spatial and visual data from high-resolution HDR imagery to enhance the interpretability of erosion and block distribution.

Table 7. Summary of average point spacing and resulting mesh complexity for each pyramid. Finer point spacing (e.g., 0.2 cm) creates denser meshes, which helps capture fine architectural details. The size and condition of the pyramid also play a role in determining the mesh's complexity.

Pyramid	Avg. Point Spacing (cm)	Approx. Triangles in Mesh Model (Million)	Notable Features Captured
Djoser	0.2	~24.3	Stepped terraces, tier deformations, casing stone erosion patterns
Unas	0.3	~10.6	Collapsed sections, preserved core masonry courses, slope remnants
Teti	0.5	~12.1	Stable lower courses, foundational alignment, measurable south-side deformation
Userkaf	0.2	~9.8	Severe erosion, block displacement, remnants of internal structural elements

The triangulation process converted billions of points into continuous surfaces of interconnected triangular facets. The final meshes achieved sub-centimeter accuracy, enabling both visual interpretation and precise quantitative analyses such as volume computation, surface erosion mapping, and morphological profiling.

An analysis of the relationship between average point spacing and mesh complexity (measured by the number of triangular facets) reveals a clear inverse trend: pyramids

scanned with finer point spacing produced significantly more mesh triangles. As shown in Figure 11, the Djoser and Userkaf models, both processed at a 0.2 cm spacing, generated the most detailed meshes with approximately 24.3 million and 9.8 million triangles, respectively. In contrast, the Unas pyramid (0.3 cm spacing) yielded ~10.6 million triangles, while the Teti pyramid, with the coarsest spacing of 0.5 cm, produced ~12.1 million triangles.

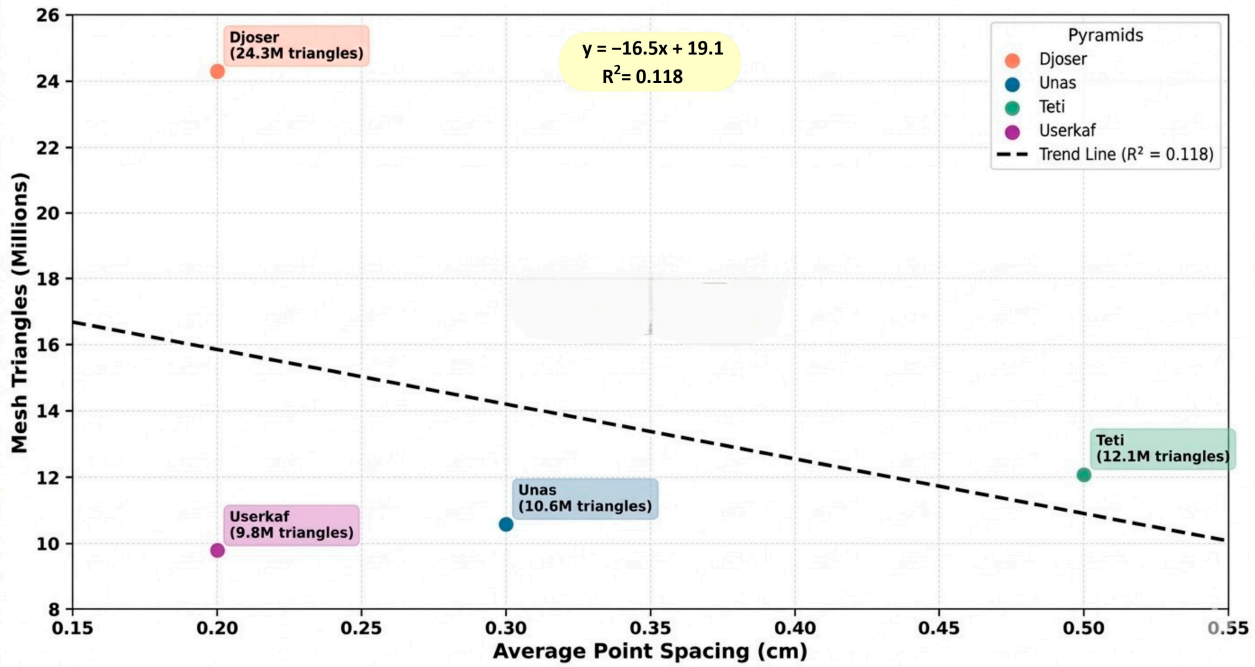

Figure 11. Relationship between average point spacing (cm) and mesh complexity. An inverse correlation is observed where finer point spacing yields more detailed meshes with a greater number of triangular facets.

This trend aligns with the theoretical expectation that higher point density creates more mesh elements during triangulation. However, the data also indicate that mesh complexity is influenced by the monument's physical size, preservation state, and structural completeness. For instance, despite having the same point spacing as Djoser, the Userkaf mesh contains fewer points due to its smaller preserved volume and extensive collapse. This relationship underscores the importance of optimizing point spacing based on both structural scale and conservation condition to balance geometric fidelity with processing efficiency in heritage documentation workflows.

The generated 3D mesh models provided detailed and structurally interpretable representations of each pyramid, enabling specific morphological analyses. The Djoser Step Pyramid model, the most complex in the dataset, reproduced the stepped terraces with exceptional detail, which allowed for deformation mapping at a sub-centimeter level (Figure 12a). Despite its heavy collapse, the Unas pyramid yielded a coherent mesh suitable for reconstructing its original slope profile (Figure 12b).

Teti's point cloud model (Figure 9) was particularly effective at capturing the lower courses, exhibiting crisp masonry block boundaries that allowed for precise analysis of its foundational structure. The complementary mesh model (Figure 13a) provides the underlying geometric surface representation optimized for overall structural form assessment and contour mapping, in which the block-level boundaries visible in the point cloud are expressed as a continuous triangulated surface rather than individual block outlines consistent with the complementary analytical roles of the two representations described for the Userkaf pyramid below. Even the mesh for Userkaf, the most degraded of the

structures, was structurally informative. Three specific analytical features make this mesh particularly valuable for heritage assessment. First, erosion depth is directly readable from the mesh surface geometry: areas of deep erosion appear as concave depressions or stepped discontinuities in the triangulated surface, whose depth can be quantified by comparing local surface elevations against the estimated original block face plane, a measurement that is only possible at this precision through a sub-centimeter georeferenced mesh. Second, block distribution irregularities are visible as abrupt surface normal changes and height discontinuities between adjacent triangulated facets, indicating displaced, tilted, or partially collapsed stone blocks whose current positions deviate measurably from their original alignment. Third, the mesh geometry directly complements the RGB-colorized point cloud presented in Figure 10, which provides photorealistic colour and texture information that visually identifies stone type, weathering staining, and surface discoloration, Figure 13b provides the underlying geometric surface model that quantifies the three-dimensional extent and depth of the same erosion features. The two figures together, a point cloud for material characterization and mesh for geometric quantification, constitute a complete analytical record of the Userkaf current structural condition that neither figure alone could provide.

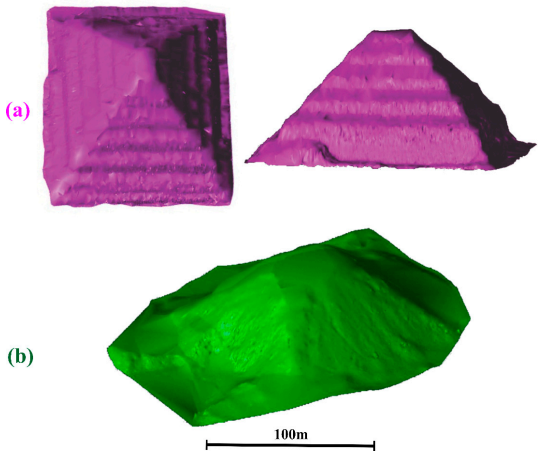

Figure 12. (**a**) Detailed 3D mesh of Djoser Pyramid showing clearly the stepped terraces and sub-centimeter deformation features, demonstrating high geometric fidelity. (**b**) 3D mesh model of Unas Pyramid capturing collapsed sections and preserved slope profiles despite significant structural damage.

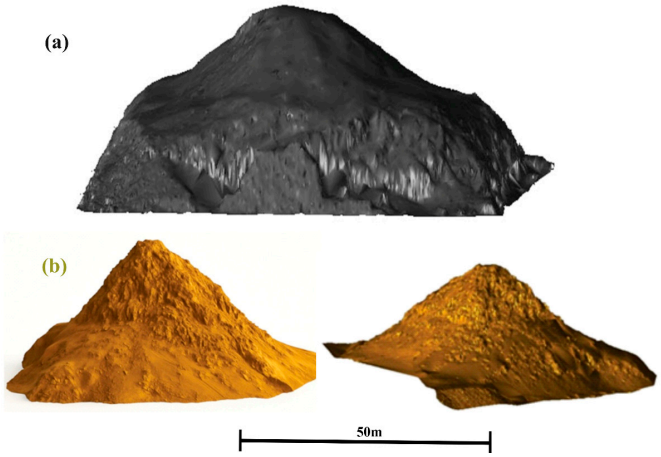

Figure 13. (**a**) Mesh representation of Teti Pyramid highlighting stable lower masonry courses and precise foundational alignment suitable for contour mapping. (**b**) Userkaf Pyramid mesh illustrating severe erosion and block displacement and remnants of architectural elements for structural interpretation.

5.3. Elevation Changes and 2D Mapping of Saqqara Pyramids

Using georeferenced 3D point cloud models of the Djoser, Unas, Teti, and Userkaf pyramids, we generated high-resolution contour maps for each monument. Contour extraction was performed based on the ellipsoidal height, later referenced to mean sea level, with vertical intervals of 0.5 m to accurately depict architectural platforms, slope gradients, and micro topographical variations. These visualizations provide clear evidence of preservation states, structural deformation, and erosion patterns that are less apparent in raw 3D views. The derived contour maps and 2D plans are vital for documentation and preservation strategies. They serve as baseline datasets for monitoring future changes, guiding stabilization interventions, and supporting public interpretation.

The apparent regularity of the contour maps for the more degraded pyramids reflects the natural geomorphology of long-term collapsed masonry in a desert environment, where millennia of debris accumulation and aeolian sand infilling produce a broadly conical mound geometry that is genuinely smooth at the 0.5–2 m contour interval scale; the block-level surface irregularities captured at sub-centimeter resolution in the TLS point clouds and mesh models (Figures 7–10, 12 and 13) are real and present, but operate at a spatial scale finer than the chosen contour interval and therefore do not appear as map-scale irregularities in the contour representation.

A comparative analysis between the current elevations and the historically documented original heights of each pyramid reveals significant losses in vertical extent over millennia due to environmental and anthropogenic factors. Published archaeological sources show that the Djoser pyramid, originally ~62.5 m [58,59], now stands at ~57 m from the base of the pyramid, indicating a minimal height loss of approximately 6% despite casing erosion (Figure 14). The contour map illustrates the elevation distribution of the Djoser Step Pyramid. The summit reaches 128 m above mean sea level (AMSL), while the pyramid base lies 71 m AMSL, showing a total vertical relief of about 57 m corresponding to the six stepped levels of the structure.

The observed ~5.5 m height reduction most likely reflects a combination of mechanisms: dominant loss of upper-tier casing stones and summit masonry through wind erosion and salt crystallization [15,59], possible minor structural settlement associated with deterioration of subsurface geological formations [11], and a contribution from aeolian sediment accumulation at the pyramid base raising the apparent ground level. Separating these contributions quantitatively would require geotechnical subsidence monitoring and ground-penetrating radar profiling of base sediment depth investigations that the georeferenced TLS baseline established by this study is specifically designed to support in future monitoring campaigns.

In stark contrast, the other pyramids have suffered far more substantial degradation. The Unas pyramid has lost over 53% of its height, reduced from an original ~43 m to a current height of ~20 m [60], primarily due to the collapse of its upper tiers and core exposure (Figure 15). The contour map of the Unas Pyramid shows that the current apex reaches approximately 90 m AMSL. The degradation is even more severe for the Teti pyramid, which has lost over 66% of its height, declining from ~52.5 m to ~18 m and now resembling a pile of stones [60,61] (Figure 16). The contour pattern of the Teti Pyramid reveals a maximum elevation of approximately 88 m AMSL, with a flattened topography resulting from extensive material loss. The gentle slope around the core indicates that most of the outer casing stones have completely eroded or collapsed. Similarly, the Userkaf pyramid has been reduced by over 63%, from an original height of ~49 m to ~18 m, now existing as a severely ruined heap of disarticulated blocks with an almost complete loss of its superstructure [60] (Figure 17). The Userkaf Pyramid exhibits a maximum elevation of about 84 m AMSL. The irregular contour distribution reflects the advanced

stage of structural erosion, leaving only a low mound of core masonry and debris. Also, climatic effects, including wind erosion, temperature-driven stone fatigue, and episodic flooding, combined with human activities such as stone quarrying and the historical reuse of materials, have accelerated deterioration. Userkaf represents the most extreme case, where the surviving form is an amorphous rubble mound with minimal architectural definition.

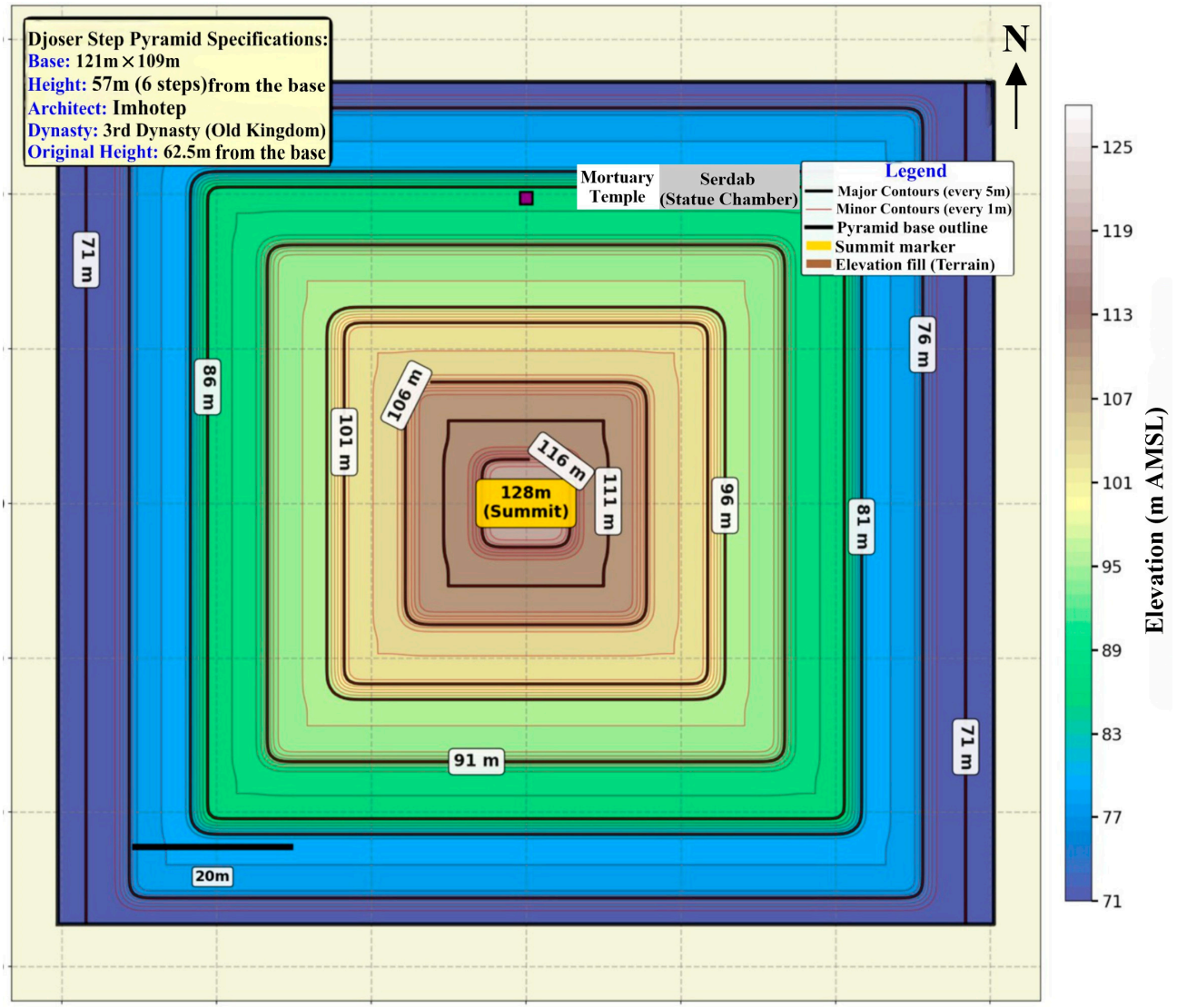

Figure 14. Contour map for Djoser Step Pyramid, Saqqara, showing six stepped platforms as defined by major (5 m) and minor (1 m) elevation intervals. The model illustrates the pyramid's reduction from its original height of 62.5 m to 57 m, with surface variations and restoration-visible layers documented through high-accuracy georeferenced point cloud data.

In addition to the 3D models, 2D plan drawings were generated from the processed point clouds for each pyramid using a custom Python 3.13.2 workflow implemented with the Open3D and NumPy libraries. The workflow comprised four sequential steps: (1) horizontal slice extraction, in which all points within a 0.3 m vertical band at the elevation of the lowest surviving masonry course were isolated from the full georeferenced point cloud; (2) orthographic projection, in which the extracted points were projected onto a horizontal plane to produce a 2D point density map representing the top-down footprint of the surviving structure; (3) boundary detection, in which the outer perimeter of the projected point cluster was computed using a convex hull algorithm applied to the densest

point concentrations, identifying the surviving wall face locations; and (4) dimensional annotation, in which wall lengths were computed as the Euclidean distances between detected corner points in the UTM coordinate system and annotated directly on the plan. No manual drafting, geometric reconstruction, or external reference data were used in any step of this process. The wall outlines and dimensions are computed directly and exclusively from the measured TLS point coordinates. The labelled feature locations (entrances, structural boundaries) were identified from the point cloud geometry and validated against published archaeological records [7,54,58,61–63].

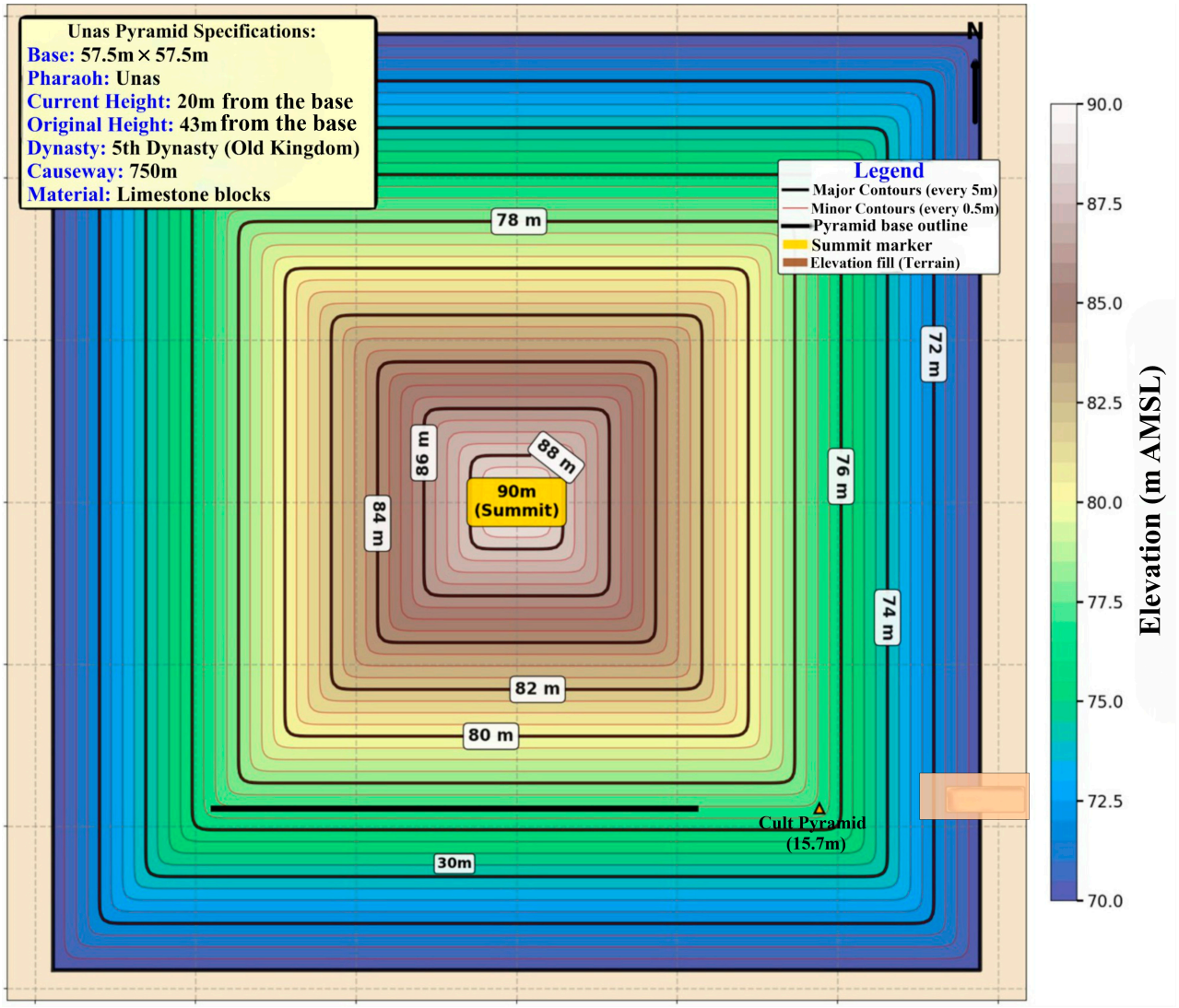

Figure 15. Contour map for the Unas Pyramid with contours at 2 m and 0.5 m intervals. This figure highlights steep slope angles, the contrast between original (43 m) and current (20 m) heights.

The schematic appearance of the plans is a deliberate and functional characteristic precisely because the plans are geometrically clean, dimensionally accurate, and georeferenced; they are directly usable as working documents by conservation engineers and site managers without requiring specialist 3D software. Their specific conservation management functions are: (i) providing a dimensionally accurate baseline footprint for each pyramid against which future surveys can detect horizontal displacement or loss of base course blocks through direct coordinate comparison; (ii) defining the precise perimeter boundaries of each structure for the establishment of conservation buffer zones and access control planning; (iii) enabling the calculation of structural footprint areas that, combined

with the volumetric data from the mesh models, allow quantification of the ratio of surviving volume to original volume for each pyramid a direct metric for degradation severity; and (iv) providing GIS-ready vector layers that can be directly overlaid with satellite imagery, geotechnical data, and conservation intervention records in heritage management GIS platforms.

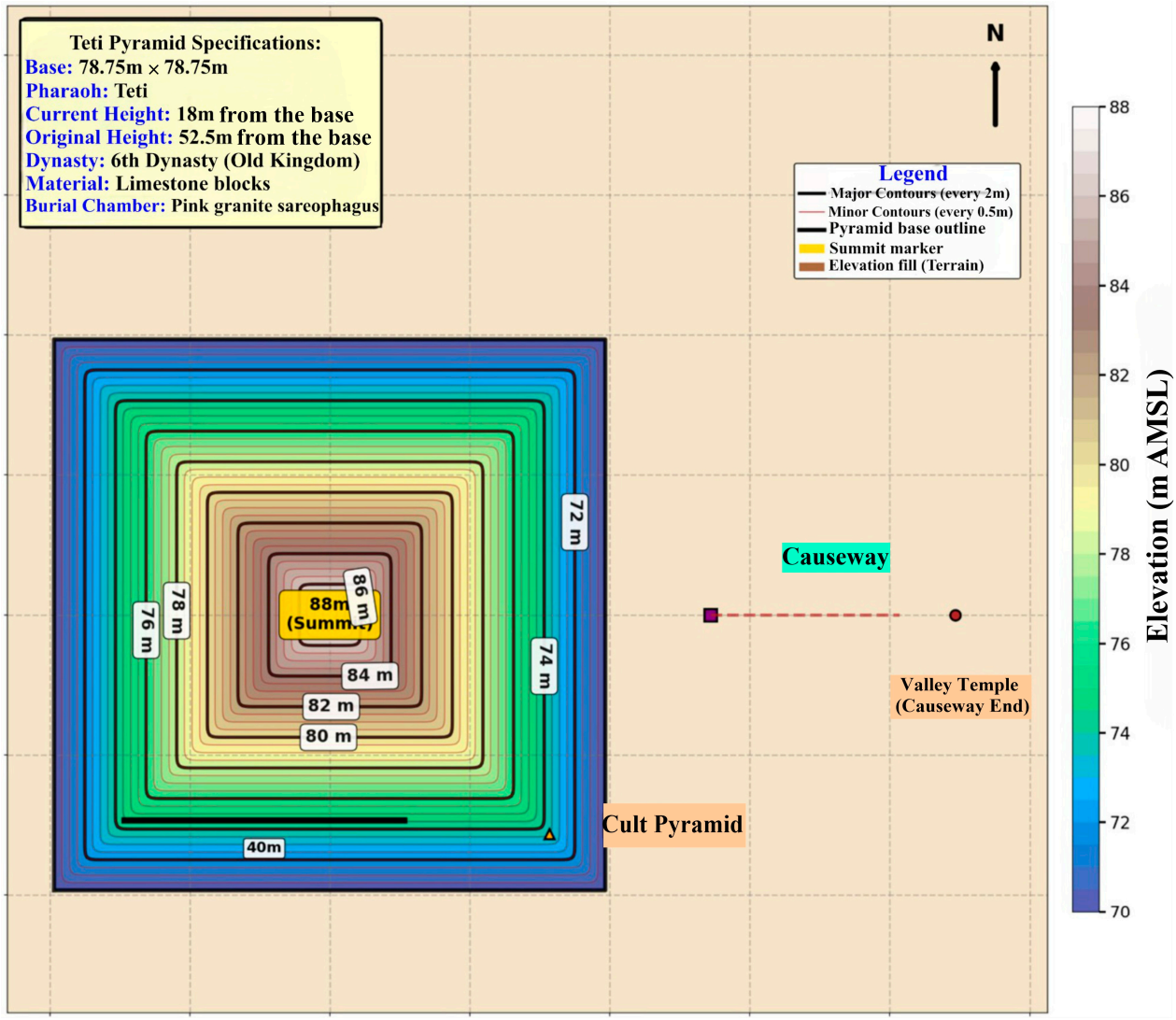

Figure 16. Contour map for the Teti Pyramid, featuring elevation bands at every 2 m and 0.5 m. The remaining central core and the drastically lowered profile (from 52.5 m to 18 m) are seen, capturing the extent of upper-layer loss and surface degradation due to environmental effects.

For the well-preserved Djoser pyramid, the resulting 2D plan offers a clear representation of its complex, multi-tiered base and surrounding structures, serving as a reliable architectural blueprint (Figure 18). In the case of the degraded Unas and Teti pyramids, the 2D plans are crucial for documenting the extent of their collapse and defining the boundaries of their remaining foundational courses, which are often obscured on the ground (Figures 19 and 20). For the Userkaf pyramid, which exists as a fragmented heap of blocks, the 2D plan is particularly valuable for mapping the distribution of disarticulated structural elements and identifying the remnants of its original footprint amidst the debris (Figure 21). As precise and scalable products, these 2D maps are suitable for direct integration into GIS platforms and are foundational for developing effective conservation management plans.

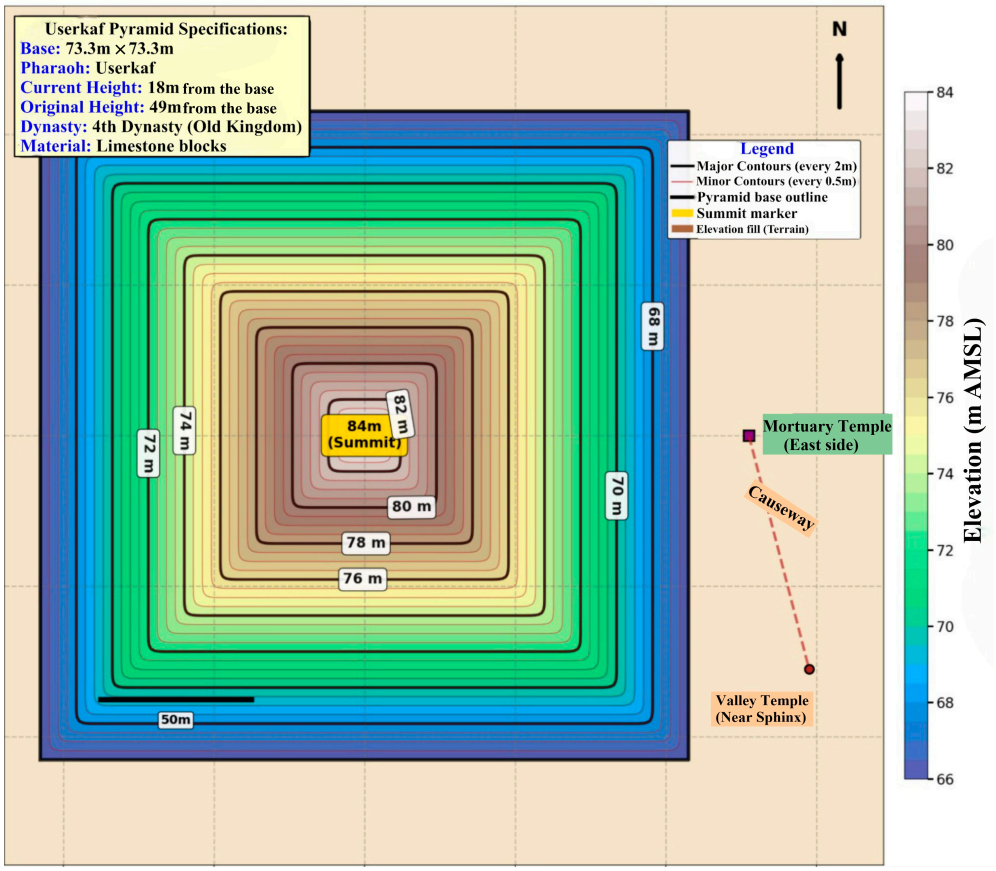

Figure 17. Contour map for the Userkaf Pyramid, displaying its transformation to a mound-like structure. Contours at 2 m and 0.5 m reveal surviving apex stones and major collapse, emphasizing reduction from the original 49 m to the present 18m.

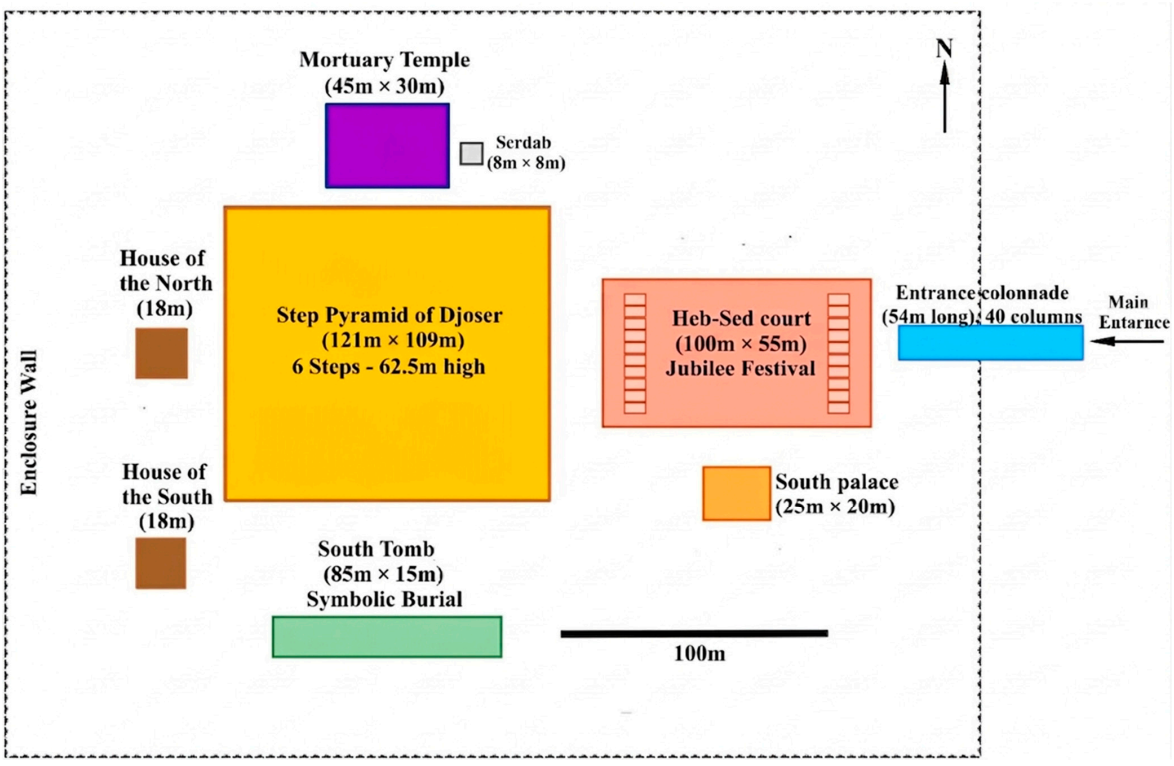

Figure 18. Two-dimensional plan of the Djoser Pyramid derived from georeferenced TLS point cloud, with annotated true wall lengths and entrance location [7,58].

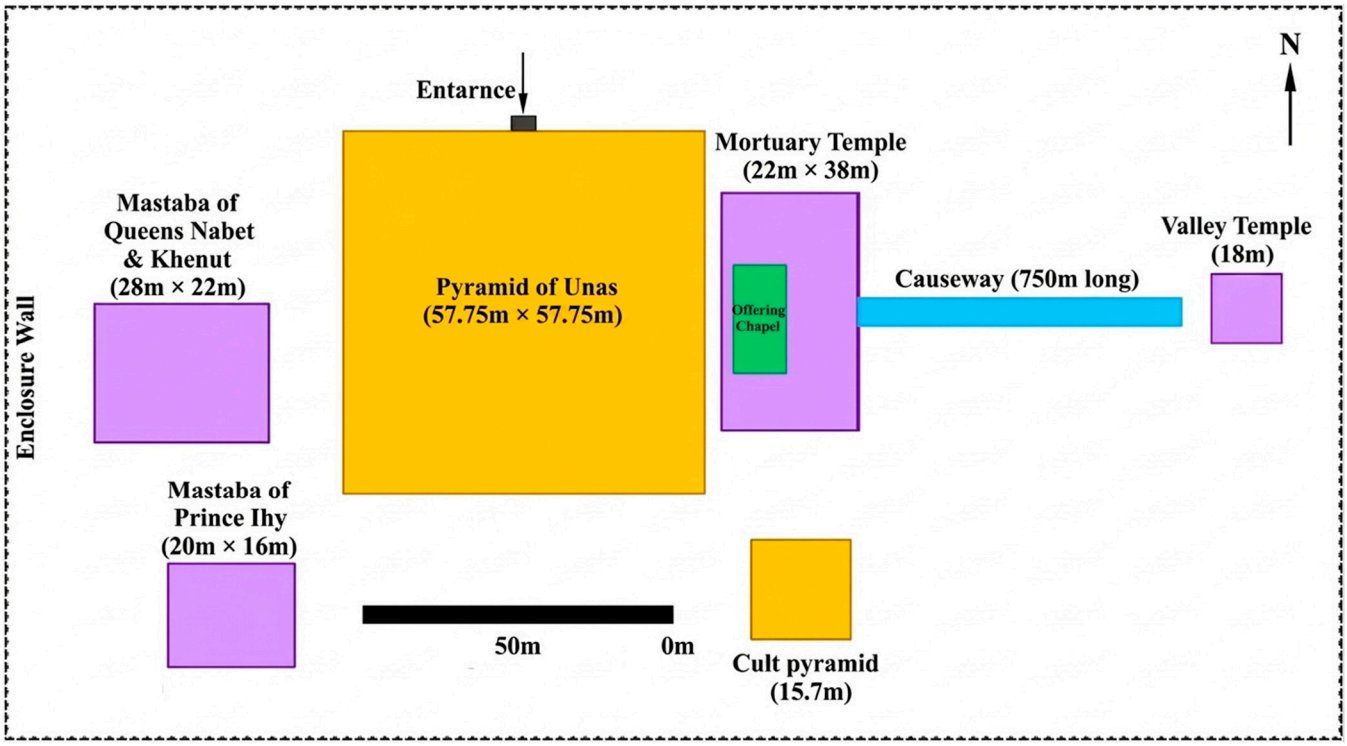

Figure 19. Two-dimensional plan of the Unas Pyramid footprint with annotated true wall lengths and entrance location [54,62].

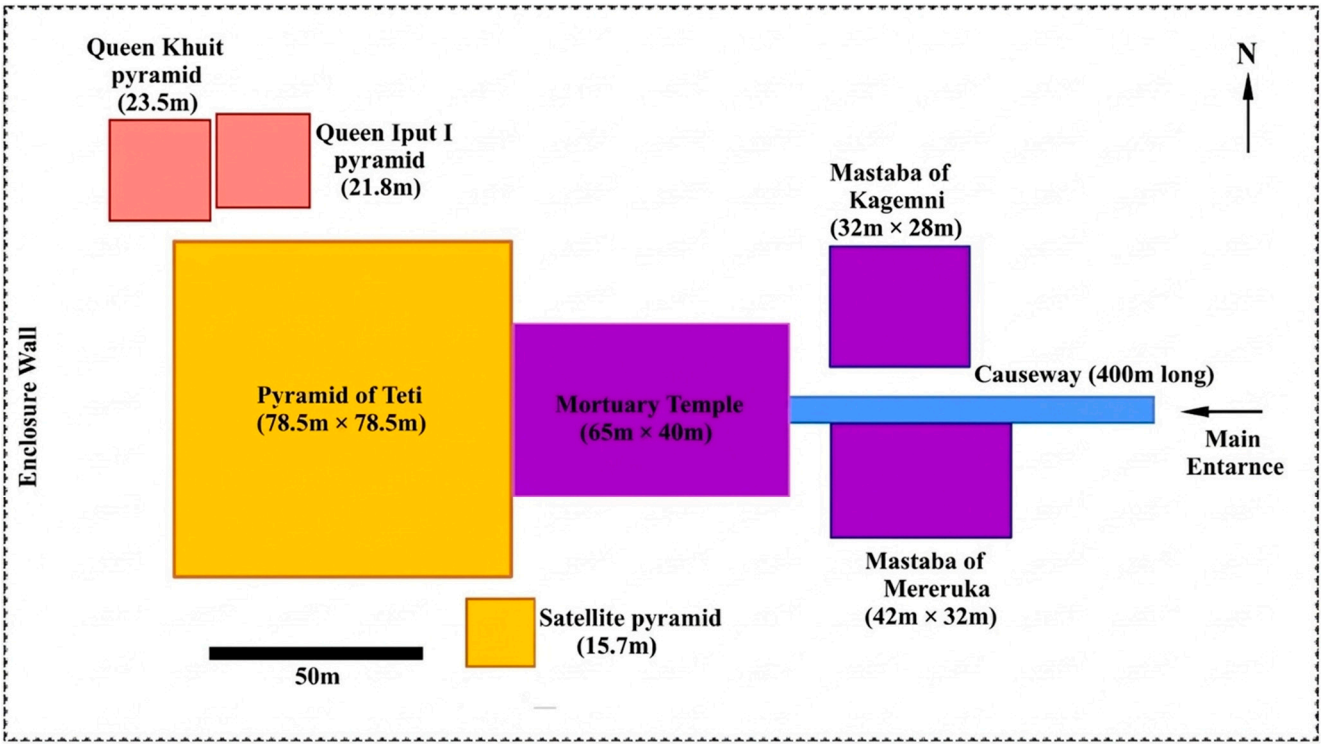

Figure 20. Two-dimensional plan of the Teti Pyramid base, with annotated true wall lengths [61].

The 2D plans generated in this study therefore represent the first georeferenced, metric-accurate orthographic documentation of all four pyramid footprints, providing a directly GIS-integrable and conservation-actionable product that supersedes all prior manually produced architectural drawings in both geometric precision and spatial referencing, while

simultaneously enabling direct quantitative comparison with published archaeological dimensional records [7,54,58,61–63].

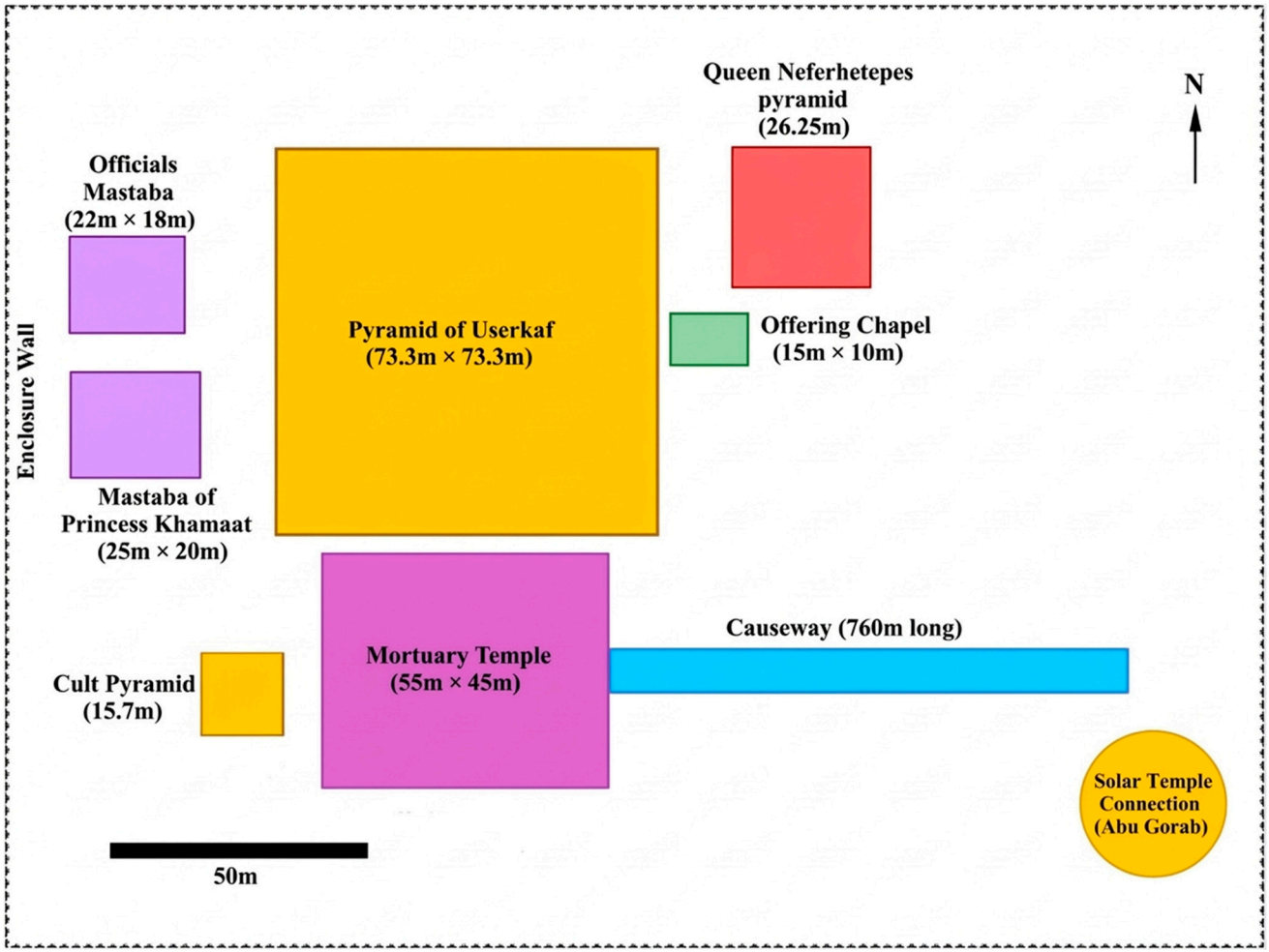

Figure 21. Two-dimensional plan of the Userkaf Pyramid remains, with annotated true wall lengths [63].

6. Discussion

The comprehensive 3D digital documentation of the Djoser Step Pyramid and the pyramids of Unas, Teti, and Userkaf at Saqqara, achieved through the integration of TLS with high-precision GNSS and Total Station control, represents a significant advancement in heritage preservation. Sub-centimeter residual registration errors (2.97 mm at Djoser, 2.96 mm at Unas, 2.98 mm at Teti, and 2.89 mm at Userkaf) confirm the exceptional spatial fidelity and reliability of the datasets. The robust georeferencing, anchored to a GNSS/Total Station control network whose accuracy was formally assessed through constrained least-squares adjustment yielding primary GCP standard deviations of ±3–4 mm horizontal and ±5–7 mm vertical, with overall 3D model accuracy estimated at ±10–12 mm through combined error propagation, facilitating integration with existing archaeological site plans, remote sensing imagery, and future monitoring surveys [64,65]. This addresses a critical challenge in managing complex, multi-layered archaeological landscapes like Saqqara, where traditional documentation methods often fall short.

From these high-resolution point clouds, a suite of critical digital products was derived, including 3D mesh models with triangular elements, contour maps, orthoimages with 1–2 cm per pixel resolution, Digital Elevation Models (DEMs), and cross-sections. These outputs are not merely visual representations but serve as foundational datasets for

various analytical applications in heritage management. The estimated preserved structural volumes (approximately 330,000 m^3 for Djoser, 120,000 m^3 for Unas, 150,000 m^3 for Teti, and 95,000 m^3 for Userkaf) provide quantitative baseline data for monitoring future degradation and planning conservation interventions.

Interpretation of these products revealed distinct preservation trajectories among the four pyramids. The Step Pyramid of Djoser retains a remarkably intact stepped form, with volumetric reduction limited to approximately 6% of its original height. The clarity of stepped terraces captured in the mesh underscores the resilience of its construction and prior restoration interventions. In contrast, the Teti pyramid exhibits localized deformation of up to 4.2 cm on its southern flank, indicative of foundation instability or historical seismic activity. The Unas pyramid, with over 53% height loss, presented a more challenging documentation case. Although the Teti Pyramid has lost about 66% of its original height, the Userkaf Pyramid shows an even more advanced stage of deterioration. Userkaf has lost approximately 63% of its initial height; however, the extent of its structural damage is significantly greater, with the loss affecting not only its height but also most of its superstructural integrity. This condition is comparable to heavily quarried sectors at Abusir and the erosion-dominated façades at Petra. Most of its outer casing stones have been completely removed, exposing the core masonry, where many blocks are now displaced or missing but the extent of its structural damage is far greater [42,60,66]. The upper sections of the pyramid have collapsed almost entirely, forming a large mound of rubble around its base. This combination of significant height loss, severe structural failure, and the disappearance of its original geometric shape clearly indicates that the Userkaf Pyramid is in a more advanced stage of degradation than the Teti Pyramid.

This study expands upon global TLS heritage documentation efforts. Previous applications at sites such as Machu Picchu [23], Petra [24], and various medieval European monuments [36] have demonstrated the power of TLS for capturing complex surfaces and monitoring structural stability. The Saqqara study contributes uniquely by integrating multi-pyramid 3D documentation within one of Egypt's most historically layered necropolises. The spatial fidelity achieved is highly comparable to that reported in leading international TLS heritage documentation studies.

Furthermore, the comparative analysis of four pyramids allows assessment of preservation states, construction techniques, and material degradation across dynastic boundaries within a single location. This multi-site perspective offers richer interpretive value, providing a broader understanding of degradation patterns and structural vulnerabilities over time. For instance, the varying degrees of height loss and structural integrity observed among the Djoser, Unas, Teti, and Userkaf pyramids offer insights into the long-term impacts of environmental factors and human activity on ancient monumental architecture.

The high-resolution 3D models allow precise quantification of degradation phenomena, such as the significant height loss in Unas, Teti, and Userkaf and the localized deformation in Teti. This level of quantitative analysis is crucial for prioritizing conservation efforts and developing targeted intervention strategies, a need echoed in studies on heritage vaults and other historic structures susceptible to deformation [67], and in parametric 3D reconstruction approaches applied to complex architectural heritage typologies [68].

The principal contributions of this study to the field of heritage geomatics and archaeological documentation can be summarized as follows. First, this study presents the first high-resolution, fully georeferenced TLS documentation of all four major pyramids at the Saqqara necropolis Djoser, Unas, Teti, and Userkaf within a single integrated survey anchored to the Egyptian Survey Authority national geodetic reference frame, producing over 2.1 billion points with sub-centimeter registration accuracy. Second, the study delivers the first quantitative TLS based assessment of height loss, volumetric change, and structural

deformation for these monuments, establishing numerically grounded baselines including a 4.2 cm localized deformation at Teti's southern flank and height losses of 53%, 66%, and 63% at Unas, Teti, and Userkaf, respectively, that were previously unavailable at this level of geometric precision. Third, the integrated geomatics workflow combining GNSS, Total Station, and TLS within a hierarchical two-tier control network demonstrates a scalable, transferable framework applicable to other large multi-monument archaeological sites worldwide where simultaneous documentation of several structures within a shared geodetic reference frame is required. Fourth, the suite of derived products, georeferenced point clouds, texture-mapped mesh models, DEMs, orthoimages, contour maps, and GIS-ready 2D plans, constitutes a comprehensive multi-format digital archive that directly serves the needs of conservation practitioners, structural engineers, archaeologists, and heritage managers [60,61].

Despite these contributions, several limitations of the present study should be acknowledged to guide future work. First, all Total Station-measured targets were used as registration constraints, and no independent checkpoints were withheld for external validation. Consequently, the accuracy estimates reported registration RMSE of 2.89–2.98 mm per pyramid and overall model accuracy of $\pm$10–12 mm from combined error propagation represent internally derived quality indicators rather than externally validated accuracy statements in the strict sense of recognized geospatial accuracy standards such as ASPRS, NSSDA, or STANAG 2215. Second, the survey was limited to the external surfaces of the four pyramids; the interior chambers and passages, where accessible, were not documented in this campaign due to logistical and access constraints. Interior TLS documentation would substantially enrich the structural dataset and should be considered in future phases. Third, the current dataset represents a single-epoch survey, providing a precise baseline but not yet enabling change detection or deformation monitoring over time. The full value of the georeferenced digital twins established by this study will be realized through repeated surveys at regular intervals, which will allow detection of progressive structural changes and support evidence-based conservation interventions. More critically, the near collinearity of the primary GNSS network was effectively mitigated by the Total Station densification of approximately 32 secondary points, which are distributed in a genuinely two-dimensional pattern around and between the pyramids, providing the geometric redundancy and cross-network constraints that the primary GNSS network alone could not supply. This hierarchical design, accepting a geometrically constrained primary network while compensating through dense two-dimensional local densification, is a recognized and practical approach in heritage survey contexts where site access restricts ideal network configuration.

Ultimately, this work affirms the indispensable role of TLS in cultural heritage conservation. The generated 'digital twins' of the Saqqara pyramids enable advanced visualization and analysis, establish invaluable baseline records for conservation, facilitate virtual dissemination, and support non-invasive restoration planning. By contributing detailed, accurate, and interoperable digital models to the global repository of heritage documentation, this study safeguards and enhances understanding of Saqqara's cultural legacy, setting a precedent for similar large-scale heritage documentation projects worldwide. This comprehensive approach provides a robust framework for future monitoring, enabling the detection of subtle changes over time and facilitating proactive conservation measures, ensuring the long-term preservation of these iconic monuments.

7. Conclusions

This study demonstrated the effectiveness of integrating TLS with high-precision geodetic control (GNSS and Total Station) for the comprehensive 3D documentation of four

iconic pyramids in Saqqara: Djoser, Unas, Teti, and Userkaf. The resulting georeferenced point clouds establish a robust digital baseline for long-term monitoring and conservation. Derived digital products, including 3D mesh models, orthoimages, DEMs, and 2D plans, offer new opportunities to evaluate preservation status, structural integrity, and degradation patterns with an unprecedented level of detail.

The derived digital products collectively provide a multi-format conservation resource whose utility extends from structural analysis to climate risk assessment and virtual dissemination. By analyzing multiple monuments within the same necropolis, the study further illustrates how environmental and anthropogenic pressures have differently impacted pyramids of varying construction styles and periods, from the relatively stable Djoser complex to the heavily eroded Unas, Teti, and Userkaf.

Beyond the regional context, the outcomes contribute to the broader field of cultural heritage management by delivering high-fidelity, reproducible records suitable for structural analysis, non-invasive restoration planning, and climate- and environment-related risk assessment. These models also enhance accessibility through virtual dissemination and provide a permanent digital archive for future interdisciplinary research.

Overall, the findings underscore the potential of advanced geomatics technologies to address the challenges of documenting, monitoring, and protecting heritage structures exposed to environmental change and human activity. The approach sets a precedent for large-scale digital documentation in complex archaeological contexts and supports the systematic integration of TLS-based workflows into global strategies for sustainable heritage conservation.

Our study supports several United Nations Sustainable Development Goals (SDGs), particularly SDG 11 (Sustainable Cities and Communities), by enhancing the protection and safeguarding of cultural heritage through precise digital documentation and monitoring. It also contributes to SDG 13 (Climate Action) by enabling climate-related risk assessment and resilience planning, and to SDG 9 (Industry, Innovation and Infrastructure) through the application of advanced geomatics technologies for sustainable heritage conservation.

Author Contributions: Conceptualization, A.E. and A.M.; methodology, A.E. and A.M.; software, A.E.; validation, I.M.I.; formal analysis, A.E. and A.M.; investigation, A.E.; resources, A.E. and I.M.I.; data curation, A.E.; writing—original draft preparation, A.E.; writing—review and editing, A.M. and I.M.I.; visualization, A.E. and I.M.I.; supervision, A.M.; project administration, I.M.I.; funding acquisition, A.E. and I.M.I. All authors have read and agreed to the published version of the manuscript.

Funding: This research received no external funding.

Data Availability Statement: The original contributions presented in this study are included in the article. Further inquiries can be directed to the first author.

Acknowledgments: The authors gratefully acknowledge the support of the Ministry of Tourism and Antiquities of Egypt for facilitating access to the Saqqara site and providing the necessary assistance during the fieldwork. Their collaboration was invaluable in enabling the successful completion of this study.

Conflicts of Interest: The authors declare no conflicts of interest.

Abbreviations

The following abbreviations are used in this manuscript:

AMSL	Above Mean Sea level
ASPRS	American Society for Photogrammetry and Remote Sensing
BCE	Before Common Era

DEM	Digital Elevation Model
CORS	Continuously Operating Reference Station
GCP	Ground control point
GIS	Geographic Information System
GNSS	Global Navigation Satellite System
HDR	High dynamic range
ICP	Iterative Closest Point
ISO	International Organization for Standardization
NSSDA	National Standard for Spatial Data Accuracy
PDOP	Position Dilution of Precision
RGB	Red, Green, and Blue
RMSE	Root Mean Squared Error
SDG	Sustainable Development Goal
STANAG	Standardization Agreement (NATO)
TBC	Trimble Business Center
TLS	Terrestrial Laser Scanning
UNESCO	United Nations Educational, Scientific and Cultural Organization
UTM	Universal Transverse Mercator
WGS84	World Geodetic System 1984

Appendix A

Table A1. UTM Zone 36N coordinates (WGS84) of the 32 Total Station-derived secondary control points and scan registration targets, grouped by pyramid zone. Point IDs follow the convention: D = Djoser, UN = Unas, T = Teti, US = Userkaf.

Point ID	Pyramid Zone	Easting (m)	Northing (m)	Height (m)	Position Relative to Pyramid
D-01	Djoser	327,832.450	3,306,312.680	69.215	North face, NW corner
D-02	Djoser	327,878.320	3,306,298.540	69.087	North face, NE corner
D-03	Djoser	327,893.670	3,306,248.390	68.743	East face, NE corner
D-04	Djoser	327,889.140	3,306,198.760	68.512	East face, SE corner
D-05	Djoser	327,848.920	3,306,178.430	68.334	South face, SE corner
D-06	Djoser	327,808.650	3,306,183.270	68.621	South face, SW corner
D-07	Djoser	327,791.380	3,306,231.540	68.896	West face, SW corner
D-08	Djoser	327,796.240	3,306,278.910	69.102	West face, NW corner
UN-01	Unas	327,558.730	3,306,091.840	73.654	North face, NW corner
UN-02	Unas	327,604.580	3,306,085.270	73.521	North face, NE corner
UN-03	Unas	327,621.340	3,306,048.930	73.298	East face, NE corner
UN-04	Unas	327,618.870	3,306,008.640	73.187	East face, SE corner
UN-05	Unas	327,597.430	3,305,986.510	73.076	South face, SE corner
UN-06	Unas	327,558.920	3,305,991.380	73.143	South face, SW corner
UN-07	Unas	327,541.670	3,306,024.760	73.312	West face, SW corner
UN-08	Unas	327,544.190	3,306,063.450	73.468	West face, NW corner
T-01	Teti	327,661.840	3,305,641.270	70.812	North face, NW corner
T-02	Teti	327,708.920	3,305,636.580	70.743	North face, NE corner
T-03	Teti	327,728.450	3,305,598.340	70.621	East face, NE corner

Table A1. *Cont.*

Point ID	Pyramid Zone	Easting (m)	Northing (m)	Height (m)	Position Relative to Pyramid
T-01	Teti	327,661.840	3,305,641.270	70.812	North face, NW corner
T-02	Teti	327,708.920	3,305,636.580	70.743	North face, NE corner
T-03	Teti	327,728.450	3,305,598.340	70.621	East face, NE corner
T-04	Teti	327,725.670	3,305,554.870	70.489	East face, SE corner
T-05	Teti	327,701.230	3,305,532.410	70.312	South face, SE corner
T-06	Teti	327,657.890	3,305,537.960	70.387	South face, SW corner
T-07	Teti	327,638.540	3,305,574.320	70.498	West face, SW corner
T-08	Teti	327,641.780	3,305,618.940	70.654	West face, NW corner
US-01	Userkaf	327,403.560	3,305,264.730	74.698	North face, NW corner
US-02	Userkaf	327,448.730	3,305,259.840	74.621	North face, NE corner
US-03	Userkaf	327,466.890	3,305,224.180	74.512	East face, NE corner
US-04	Userkaf	327,463.540	3,305,182.650	74.389	East face, SE corner
US-05	Userkaf	327,440.280	3,305,160.430	74.276	South face, SE corner
US-06	Userkaf	327,398.750	3,305,165.870	74.312	South face, SW corner
US-07	Userkaf	327,381.640	3,305,199.540	74.401	West face, SW corner
US-08	Userkaf	327,384.920	3,305,241.870	74.534	West face, NW corner

References

1. Mamo, A.R.; Ibraheem, I.M.; Al Kassem, A.; Al-Khalil, A.; Hopper, K. The Impact of the Syrian Conflict on Archaeological Sites in Al-Hasakah Province. *J. Archaeol. Sci. Rep.* **2022**, *43*, 103486. [CrossRef]
2. Elbshbeshi, A.; Gomaa, A.; Mohamed, A.; Othman, A.; Ibraheem, I.M.; Ghazala, H. Applying Geomatics Techniques for Documenting Heritage Buildings in Aswan Region, Egypt: A Case Study of the Temple of Abu Simbel. *Heritage* **2023**, *6*, 742–761. [CrossRef]
3. Al Kassem, A.; Hopper, K.; Ibraheem, I.M.; el Hajj, H.; Maier, A.; Ali, A.A.; Richter, J. Assessment of the impact of the Syrian conflict on archaeological sites in the Daraa region. *Levant* **2024**, *56*, 425–446. [CrossRef]
4. Koukouvelas, I.K.; Kyriou, A.; Nikolakopoulos, K.G.; Dimaris, G.; Pantelidis, I.; Tsikos, H. Geological and 3D Image Analysis Toward Protecting a Geosite: The Case Study of Falakra, Limnos, Greece. *Minerals* **2025**, *15*, 148. [CrossRef]
5. Kyriou, A.; Filippa, T.; Pappas, C.; Nikolakopoulos, K.G.; Koukouvelas, I. Generation of high-quality 3D models of a monastery located in Western Greece. In *Earth Resources and Environmental Remote Sensing/GIS Applications*; SPIE: Bellingham, WA, USA, 2023; Volume 12734, pp. 99–111. [CrossRef]
6. Landreau, X.; Piton, G.; Morin, G.; Bartout, P.; Touchart, L.; Giraud, C.; Barre, J.-C.; Guerin, C.; Alibert, A.; Lallemand, C. On the possible use of hydraulic force to assist with building the step pyramid of saqqara. *PLoS ONE* **2024**, *19*, e0306690. [CrossRef]
7. Hawass, Z. The Discovery of the Sarcophagus of Djoser and the Restoration of the Step Pyramid. *J. Gen. Union Arab Archaeol.* **2021**, *6*, 83–107. [CrossRef]
8. Lauer, J.P. *Saqqara: The Royal Cemetery of Memphis: Excavations and Discoveries Since 1850*; Scribner: New York, NY, USA, 1976.
9. Staring, N. *The Saqqara Necropolis Through the New Kingdom: Biography of an Ancient Egyptian Cultural Landscape*; Brill: Leiden, The Netherlands, 2022; Volume 131.
10. Mysliwiec, K.J. *In the Shadow of Djoser's Pyramid: Research of Polish Archaeologists in Saqqara*; Peter Lang International Academic Publishers: New York, NY, USA, 2020; p. 478.
11. La Torre, C. Risk Assesment of the Archaelogical Site of Saqqara. In *North Saqqara Archaeological Site: Handbook for the Environmental Risk Analysis*; Abdelrahman, M., Ed.; Consiglio Nazionale delle Ricerche (CNR), Istituto per le Tecnologie Applicate ai Beni Culturali: Rome, Italy, 2003; pp. 1000–1024. [CrossRef]
12. Fahmy, A.; Molina-Piernas, E.; Domínguez-Bella, S.; Martínez-López, J.; Helmi, F. Geoenvironmental investigation of Sahure's pyramid, Abusir archeological site, Giza, Egypt. *Herit. Sci.* **2022**, *10*, 61. [CrossRef]

13. Soliman, M.; Ali, D.; Elbshbeshi, A.; Ibrahim, M.G. Digitization of Qaitbay Fort in Alexandria (884AH/ 1479 CE) -Simplification of Modelling Techniques to Safeguard Vulnerable Cultural Heritage. *Art Res. J.* **2025**, *25*, 109–121.
14. Yilmaz, Y.; Gamil, R.E. The role of heritage impact assessment in safeguarding World Heritage Sites: Application study on historic areas of Istanbul and Giza Pyramids. *J. Herit. Manag.* **2018**, *3*, 127–158. [CrossRef]
15. Madkour, F.S.; Khallaf, M.K. Alteration processes and deterioration phenomena of faience tiles in the complex of king Djoser at Saqqara, Egypt. *Asian J. Behav. Stud.* **2013**, *3*, 25–37. [CrossRef]
16. Ewais, A.Y.; Kamal, M.; Mahgoub, G. Artistic Study of the wildlife scene at the burial chamber of Rashepses in Saqqara, Egypt. *J. Cent. Glob. Study Cult. Herit. Cult.* **2018**, *5*, 93–101. [CrossRef]
17. Mohamed, H.M.; Khamis, Z.A.E.-T.R. Diagnosis of the Deterioration and Conservation of Bes Pottery Jar from the Tomb of Petah Umm Uya in Saqqara. *Int. J. Conserv. Sci.* **2024**, *15*, 449–460. [CrossRef]
18. Elbshbeshi, A.; Gomaa, A.; Mohamed, A.; Othman, A.; Ibraheem, I.M.; Ghazala, H. Assessing the Impact of Water Level Fluctuations on Philae Island's, Aswan, Egypt Stability and Seismic Vulnerability Using Global Positioning System and Horizontal to Vertical Spectral Ratio Techniques. *Results Eng.* **2025**, *27*, 107026. [CrossRef]
19. Remondino, F. Advanced 3D recording techniques for the digital documentation and conservation of heritage sites and objects. *Change Over Time* **2011**, *1*, 198–214. [CrossRef]
20. Stylianidis, E. Recording and Documenting Cultural Heritage. In *Exploring the Ethical Dimension in Recording and Documenting Cultural Heritage*; Springer: Berlin/Heidelberg, Germany, 2025; pp. 25–46. [CrossRef]
21. Kyriou, A.; Nikolakopoulos, K.; Koukouvelas, I. How image acquisition geometry of UAV campaigns affects the derived products and their accuracy in areas with complex geomorphology. *ISPRS Int. J. Geo-Inf.* **2021**, *10*, 408. [CrossRef]
22. Sammartano, G.; Spanò, A. Point clouds by SLAM-based mobile mapping systems: Accuracy and geometric content validation in multisensor survey and stand-alone acquisition. *Appl. Geomat.* **2018**, *10*, 317–339. [CrossRef]
23. Dominika, S.; Bartłomiej, Ć.; Krzysztof, W.; Dąbek, P.B.; Bastante, J.M.; Izabela, W. Inca water channel flow analysis based on 3D models from terrestrial and UAV laser scanning at the Chachabamba archaeological site (Machu Picchu National Archaeological Park, Peru). *J. Archaeol. Sci.* **2022**, *137*, 105515. [CrossRef]
24. Alshawabkeh, Y.; Bal'awi, F.; Haala, N. 3D digital documentation, assessment, and damage quantifi cation of the Al-Deir monument in the ancient city of Petra, Jordan. *Conserv. Manag. Archaeol. Sites* **2010**, *12*, 124–145. [CrossRef]
25. Krusche, K. 3D documentation and visualization of the Forum Romanum: The DHARMA Forum Project. In *Euro-Mediterranean Conference*; Euromed: Rabat, Morocco, 2018; pp. 281–300. [CrossRef]
26. Lichti, D.D.; Glennie, C.L.; Jahraus, A.; Hartzell, P. New approach for low-cost TLS target measurement. *J. Surv. Eng.* **2019**, *145*, 04019008. [CrossRef]
27. Wu, C.; Yuan, Y.; Tang, Y.; Tian, B. Application of terrestrial laser scanning (TLS) in the architecture, engineering and construction (AEC) industry. *Sensors* **2021**, *22*, 265. [CrossRef]
28. Lemmens, M. Terrestrial Laser Scanning. In *Geo-Information: Geotechnologies and Environment*; Springer: Dordrecht, The Netherlands, 2011; pp. 101–121. [CrossRef]
29. Muralikrishnan, B. Performance evaluation of terrestrial laser scanners A review. *Meas. Sci. Technol.* **2021**, *32*, 072001. [CrossRef] [PubMed]
30. Petrovič, D.; Grigillo, D.; Kosmatin Fras, M.; Urbančič, T.; Kozmus Trajkovski, K. Geodetic methods for documenting and modelling cultural heritage objects. *Int. J. Archit. Herit.* **2021**, *15*, 885–896. [CrossRef]
31. Vileikis, O.; Khabibullaeyev, F. Application of digital heritage documentation for condition assessments and monitoring change in Uzbekistan. *ISPRS Ann. Photogramm. Remote Sens. Spat. Inf. Sci.* **2021**, *8*, 179–186. [CrossRef]
32. Rashdi, R.; Garrido, I.; Balado, J.; Del Río-Barral, P.; Rodríguez-Somoza, J.L.; Martínez-Sánchez, J. Comparative Evaluation of LiDAR systems for transport infrastructure: Case studies and performance analysis. *Eur. J. Remote Sens.* **2024**, *57*, 2316304. [CrossRef]
33. *ISO 17123-9:2018*; Optics and Optical Instruments Field Procedures for Testing Geodetic and Surveying Instruments Part 9: Terrestrial Laser Scanners. International Organization for Standardization: Geneva, Switzerland, 2018. Available online: https://www.iso.org/standard/68382.html (accessed on 29 March 2026).
34. *ISO 17123-5:2018*; Optics and Optical Instruments Field Procedures for Testing Geodetic and Surveying Instruments Part 5: Total Stations. International Organization for Standardization: Geneva, Switzerland, 2018. Available online: https://www.iso.org/standard/71689.html (accessed on 29 March 2026).
35. *ISO 17123-11:2025*; Optics and Optical Instruments Field Procedures for Testing Geodetic and Surveying Instruments Part 11: GNSS Instruments. International Organization for Standardization: Geneva, Switzerland, 2025. Available online: https://www.iso.org/standard/85271.html (accessed on 29 March 2026).
36. Golparvar-Fard, M.; Bohn, J.; Teizer, J.; Savarese, S.; Peña-Mora, F. Evaluation of image-based modeling and laser scanning accuracy for emerging automated performance monitoring techniques. *Autom. Constr.* **2011**, *20*, 1143–1155. [CrossRef]

37. Xu, Y.; Wang, Y.; Yang, J.; Zhang, J. Two-stage terrestrial laser scan planning framework for geometric measurement of civil infrastructures. *Measurement* **2025**, *242*, 115785. [CrossRef]
38. Su, K.; Jin, S.; Hoque, M.M. Evaluation of ionospheric delay effects on multi-GNSS positioning performance. *Remote Sens.* **2019**, *11*, 171. [CrossRef]
39. Li, X.; Shen, Z.; Li, X.; Liu, G.; Zhou, Y.; Li, S.; Lyu, H.; Zhang, Q. Continuous decimeter-level positioning in urban environments using multi-frequency GPS/BDS/Galileo PPP/INS tightly coupled integration. *Remote Sens.* **2023**, *15*, 2160. [CrossRef]
40. Sabzali, M.; Jazirian, I. Improvement the modelling of atmospheric effects for electronic distance measurement (EDM): Analysis of air temperature, atmospheric pressure and relative humidity of air. *Geod. Cartogr.* **2022**, *48*, 20–30. [CrossRef]
41. Treccani, D.; Adami, A.; Brunelli, V.; Fregonese, L. Mobile mapping system for historic built heritage and GIS integration: A challenging case study. *Appl. Geomat.* **2024**, *16*, 293–312. [CrossRef]
42. Grimaud, V.; Cassen, S. Implementing a protocol for employing three-dimensional representations in archaeology (PETRA) for the documentation of neolithic funeral architecture in Western France. *Digit. Appl. Archaeol. Cult. Herit.* **2019**, *13*, e00096. [CrossRef]
43. Cheng, L.; Chen, S.; Liu, X.; Xu, H.; Wu, Y.; Li, M.; Chen, Y. Registration of laser scanning point clouds: A review. *Sensors* **2018**, *18*, 1641. [CrossRef]
44. Urbančič, T.; Roškar, Ž.; Kosmatin Fras, M.; Grigillo, D. New target for accurate terrestrial laser scanning and unmanned aerial vehicle point cloud registration. *Sensors* **2019**, *19*, 3179. [CrossRef] [PubMed]
45. Zong, Y.; Liang, J.; Pai, W.; Ye, M.; Ren, M.; Zhao, J.; Tang, Z.; Zhang, J. A high-efficiency and high-precision automatic 3D scanning system for industrial parts based on a scanning path planning algorithm. *Opt. Lasers Eng.* **2022**, *158*, 107176. [CrossRef]
46. Liu, J.; Azhar, S.; Willkens, D.; Li, B. Static terrestrial laser scanning (TLS) for heritage building information modeling (HBIM): A systematic review. *Virtual Worlds* **2023**, *2*, 90–114. [CrossRef]
47. Baik, A. A Comprehensive Heritage BIM Methodology for Digital Modelling and Conservation of Built Heritage: Application to Ghiqa Historical Market, Saudi Arabia. *Remote Sens.* **2024**, *16*, 2833. [CrossRef]
48. Kaasalainen, S.; Jaakkola, A.; Kaasalainen, M.; Krooks, A.; Kukko, A. Analysis of incidence angle and distance effects on terrestrial laser scanner intensity: Search for correction methods. *Remote Sens.* **2011**, *3*, 2207–2221. [CrossRef]
49. Soudarissanane, S.; Lindenbergh, R.; Menenti, M.; Teunissen, P. Scanning geometry: Influencing factor on the quality of terrestrial laser scanning points. *ISPRS J. Photogramm. Remote Sens.* **2011**, *66*, 389–399. [CrossRef]
50. Damięcka-Suchocka, M.; Katzer, J.; Suchocki, C. Application of TLS technology for documentation of brickwork heritage buildings and structures. *Coatings* **2022**, *12*, 1963. [CrossRef]
51. Tan, K.; Cheng, X. Correction of incidence angle and distance effects on TLS intensity data based on reference targets. *Remote Sens.* **2016**, *8*, 251. [CrossRef]
52. Remondino, F.; Rizzi, A. Reality-based 3D documentation of natural and cultural heritage sites—Techniques, problems, and examples. *Appl. Geomat.* **2010**, *2*, 85–100. [CrossRef]
53. Trillo, C.; Aburamadan, R.; Mubaideen, S.; Salameen, D.; Makore, B.C.N. Towards a systematic approach to digital technologies for heritage conservation. *Insights from Jordan. Preserv. Digit. Technol. Cult.* **2020**, *49*, 121–138. [CrossRef]
54. Willkens, D.S.; Liu, J.; Alathamneh, S. A case study of integrating terrestrial laser scanning (TLS) and building information modeling (BIM) in heritage bridge documentation: The Edmund Pettus Bridge. *Buildings* **2024**, *14*, 1940. [CrossRef]
55. Remondino, F.; El-Hakim, S. Image-based 3D modelling: A review. *Photogramm. Rec.* **2006**, *21*, 269–291. [CrossRef]
56. Özkan, T.; Lavric, I.; Hochreiner, G.; Pfeifer, N. Automated 3D modeling vs. manual methods: A comparative study on historic timber tower structure assessment. *Remote Sens.* **2025**, *17*, 448. [CrossRef]
57. Liu, J.; Willkens, D.; Gentry, R. Developing a Practice-Based Guide to Terrestrial Laser Scanning (TLS) for Heritage Documentation. *Heritage* **2025**, *8*, 313. [CrossRef]
58. Hawass, Z. A fragmentary monument of Djoser from Saqqara. *J. Egypt. Archaeol.* **1994**, *80*, 45–56. [CrossRef]
59. Casas, J.E.; Cañizares, M.; Baritto, I. The Great Step Pyramid of Djoser: History, Geology and Nanoplankton Content from its Rock Casing. *J. Geol. Resour. Eng.* **2023**, *11*, 1–9. [CrossRef]
60. Ali, M.J. The Great Pyramid at Giza is a 60-degree Pyramid According to Early Authors' Writings. *Minia J. Tour. Hosp. Res.* **2022**, *14*, 91–112. [CrossRef]
61. Hamilton, J.C. Satinteti's Offering Table: A Reused Block from Princess Watetkhethor Zeshzeshet's Chapel in the Teti Pyramid Cemetery, Saqqara. *J. Egypt. Archaeol.* **2022**, *108*, 93–103. [CrossRef]
62. Hays, H.M. On the Architectural Development of Monumental Tombs South of the Unas Causeway at Saqqara from the Reigns of Akhenaten to Ramses II. *Abus. Saqqara Year* **2010**, *1*, 84–105.
63. El-Khouly, A. Excavations at the Pyramid of Userkaf, 1976: Preliminary Report. *J. Egypt. Archaeol.* **1978**, *64*, 35–43. [CrossRef]
64. Hussein, S.K.; Abdulla, K.Y. Surveying with GNSS and total station: A comparative study. *Eurasian J. Sci. Eng.* **2021**, *7*, 59–73. [CrossRef]

65. Li, X.; Zhang, X.; Ren, X.; Fritsche, M.; Wickert, J.; Schuh, H. Precise positioning with current multi-constellation global navigation satellite systems: GPS, GLONASS, Galileo and BeiDou. *Sci. Rep.* **2015**, *5*, 8328. [CrossRef]
66. Beckers, B.; Schütt, B.; Tsukamoto, S.; Frechen, M. Age determination of Petra's engineered landscape–optically stimulated luminescence (OSL) and radiocarbon ages of runoff terrace systems in the Eastern Highlands of Jordan. *J. Archaeol. Sci.* **2013**, *40*, 333–348. [CrossRef]
67. Sacco, G.L.S.; Battini, C.; Calderini, C. A case study of preliminary damage detection of two heritage vaults through geometric deformation analysis on 3D point clouds. *Structures* **2024**, *68*, 107175. [CrossRef]
68. Zhou, Y.; Zhang, M.; Li, L.; Huang, W. Parametric 3D reconstructing and interpreting iconographic evidence: Case of the Song Dynasty architectural massing typologies. *npj Herit. Sci.* **2025**, *13*, 300. [CrossRef]

Disclaimer/Publisher's Note: The statements, opinions and data contained in all publications are solely those of the individual author(s) and contributor(s) and not of MDPI and/or the editor(s). MDPI and/or the editor(s) disclaim responsibility for any injury to people or property resulting from any ideas, methods, instructions or products referred to in the content.